NOTE TO USERS

This reproduction is the best copy available.

UMI®

Design and Fabrication of Surface Textured MEMS for Infrared Gas Sensors

Liwei Sun

A Thesis

in

The Department

of

Electrical and Computer Engineering

Presented in Partial Fulfillment of the Requirements
For the Degree of Master of Applied Science at
Concordia University
Montreal, Quebec, Canada

November 2004

© Liwei Sun, 2004

Library and
Archives Canada

Published Heritage
Branch

395 Wellington Street
Ottawa ON K1A 0N4
Canada

Bibliothèque et
Archives Canada

Direction du
Patrimoine de l'édition

395, rue Wellington
Ottawa ON K1A 0N4
Canada

Your file Votre référence
ISBN: 0-494-04402-0
Our file Notre référence
ISBN: 0-494-04402-0

NOTICE:
The author has granted a non-exclusive license allowing Library and Archives Canada to reproduce, publish, archive, preserve, conserve, communicate to the public by telecommunication or on the Internet, loan, distribute and sell theses worldwide, for commercial or non-commercial purposes, in microform, paper, electronic and/or any other formats.

The author retains copyright ownership and moral rights in this thesis. Neither the thesis nor substantial extracts from it may be printed or otherwise reproduced without the author's permission.

AVIS:
L'auteur a accordé une licence non exclusive permettant à la Bibliothèque et Archives Canada de reproduire, publier, archiver, sauvegarder, conserver, transmettre au public par télécommunication ou par l'Internet, prêter, distribuer et vendre des thèses partout dans le monde, à des fins commerciales ou autres, sur support microforme, papier, électronique et/ou autres formats.

L'auteur conserve la propriété du droit d'auteur et des droits moraux qui protège cette thèse. Ni la thèse ni des extraits substantiels de celle-ci ne doivent être imprimés ou autrement reproduits sans son autorisation.

In compliance with the Canadian Privacy Act some supporting forms may have been removed from this thesis.

While these forms may be included in the document page count, their removal does not represent any loss of content from the thesis.

Conformément à la loi canadienne sur la protection de la vie privée, quelques formulaires secondaires ont été enlevés de cette thèse.

Bien que ces formulaires aient inclus dans la pagination, il n'y aura aucun contenu manquant.

ABSTRACT

Design and Fabrication of Surface Textured

MEMS for Infrared Gas Sensors

Liwei Sun

This thesis concentrates primarily on optimum design and fabrication of novel MEMS (micro-electro-mechanical systems) infrared gas sensors. It deals with the thermal, electrical, optical and mechanical response for a spectroscopic gas sensor based on MEMS surface textured technologies.

An overview of the theories of conventional and novel MEMS infrared gas sensors is presented. Two important surface modification technologies: Photonic Crystal (PC) and Surface Plasmon (SP) for the proposed devices as well as the SP dispersion relation are discussed.

The structures, materials, geometries, and electrical properties of the devices for the generation of single and narrow band mid–infrared light source with high transmission efficiency are studied. Plane Wave Methods (PWM) are used to simulate Photonic Bandgap (PBG) and Finite Difference Time Domain (FDTD) methods are used to simulate the function of the proposed devices.

Silicon on isolator (SOI) technology is used to design and fabricate the proposed device onto a microbridge that enable the power efficiency heating the device and enhance its sensitivity to gas concentration. This fabrication process (MicraGEM) provided by CMC (Canadian Microelectronics Corporation) and Micralyne Incorporation. Unfortunately, the devices could not be successfully fabricated although

our design did not break any design rule. The main reason is that the process provided error minimum size of self-alignment etching holes. However, this design help CMC and Micralyne to identify and redefine the design rules also push Micralyne to improve the process in the future.

ACKNOWLEDGEMENT

It was a great pleasure for me to work with Dr. Mojtaba Kahrizi, my supervisor, who introduced to me the concept of photonic devices and helped me to expand my knowledge in this new field; not only for sharing his broad and profound academic knowledge, but also for his extraordinarily patience, encouragement and support through my research work. Also I would like to thank him for leading me in challenging new technologies in sensor design and investigating several new processes in order to fabricate the proposed device.

I sincerely thank Dr. Victor Rossakhaty for his insightful discussions on research related problems. Meanwhile, thanks must be given to my classmates: Mr. Jun Li and Xiaohong Mu, for their timely discussion of the fabrication technologies; Mr. Jun Chen, for his help in using SEM (Scanning Electron Microscopy); and Mr. Siamak Fouladi, for his help in MEMSPro operation.

Contents

List of Figures ix

List of Tables xiii

List of Symbols xv

List of Abbreviations xvi

1 Introduction 1

1.1 Overview 1

1.2 The novel MEMS infrared gas sensors 3

1.3 Summary of the work 6

2 Theoretical background 10

2.1 Infrared absorption characteristics of common gases 10

2.2 The theory of conventional infrared gas sensor 11

2.3 The theory of MEMS infrared gas sensors 13

2.4 The theories of photonic crystal and surface plasmon 16

2.4.1 Photonic crystals 16

2.4.2 Surface plasmon 17

2.4.3 Surface plasmon dispersion relation 19

3 Optimal materials, geometries, and electrical properties for proposed devices 23

3.1 materials 23

3.2 Optimize geometry of the proposed device 26

3.2.1 The definition of the polarizations 27

3.2.2 Photonic bandgaps 27

3.2.3 Optimizing Band gap 38

3.3 Photonic crystal slabs (PCS) 42

3.3.1 Characters of light from 2D PCS structure 42

3.3.2 Enhancement of light Extraction from 2D PCS 45

3.3.3 PCS with bottom cladding 47

3.3.4 The dependence of extraction efficiency on air-hole depth 50

3.4 Optimize the electrical properties of the proposed device 51

4 Design and fabrication 54

4.1 The structures, materials and geometry parameters 54

4.1.1 The structures 54

4.1.2 Materials 54

4.1.3 Geometry parameters 55

4.2 The choice of the technology process 57

4.3 Fabrication technology and design 59

4.3.1 Fabrication processing 59

4.3.2 The advantages of MicraGEM processing for proposed device 62

4.3.3 Design of the proposed devices 63

4.4 The simulation results of our propose devices 66

4.5 Fabrication results and analysis 69

5 Conclusions, suggestions and future works 75

5.1 Conclusions 78

5.2 Suggestions 80

5.3 Future work 81

References 83

Appendix I The measurement methods for the proposed devices 88

Appendix II The FDTD Algorithm 90

List of Figures

2.1	Infrared Absorption characteristics of Common Gases	11
2.2	Distribution of light wavelengths	11
2.3	Conventional infrared gas sensors	12
2.4	The theory of MEMS infrared gas sensors	15
2.5	Two kinds of photonic crystals with a hexagonal lattice (rods/holes)	17
2.6	Surface plasmon resonance (SPR) is excited by p-polarized totally internally reflected light at a silicon /metal film interface, the surface plasmon enhances the evanescent field amplitude, E.	19
2.7	The simulation and measurement results of square arrays with square holes [6]	22
2.8	The simulation of reflectivity with different hexagonal lattice arrays of circle holes [3]	22
3.1	Dielectric influence on the width of the emission (square array) [7]	25
3.2	Light propagate in "Bar" structure photonic crystal	26
3.3	Hexagonal array with circle holes (a), square array with circle holes (b) and square holes (c)	27
3.4	hexagonal array with air holes	28
3.5	Brillouin zone and Kpath	28

3.6	TE PBG for hexagonal array of air holes (r=0.25a)	29
3.7	TM PBG for hexagonal array of air holes (r=0.25a)	30
3.8	TE PBG for hexagonal array of air holes (r=0.3a)	31
3.9	TM PBG for hexagonal array of air holes (r=0.3a)	31
3.10	Square array with circle air holes	32
3.11	Brillouin zone and K path	32
3.12	TE PBG of square array with circle air holes (r=0.4a)	32
3.13	TM PBG of square array with circle air holes (r=0.4a)	33
3.14	TE PBG of square array with circle air holes (r=0.28a)	34
3.15	TM PBG of square array with circle air holes (r=0.28a)	34
3.16	Square arrays with square holes	35
3.17	Brillouin zone of square Array	35
3.18	TE PBG of square array with square air holes (w=0.6a)	35
3.19	TM PBG of square array with square air holes (w=0.6a)	36
3.20	TE PBG of square array with square air holes (w=0.75a)	36
3.21	TE PBG of square array with square air holes (w=0.56a)	37
3.22	TE/TM Band Map and Gaps of hexagonal array with air holes	39
3.23	TE/TM Band Map and Gaps of square array with circle air holes	40
3.24	TE/TM Band Map and Gaps of square array with square air holes	41
3.25	Photonic Crystal Slabs (PBS)	43
3.26	Even/odd of Photonic Crystal Slabs	44
3.27	(a) uniform dielectric slab (b) Wave vector ($2\pi/a$) (c) Output efficiency	46
3.28	(a) Photonic crystal slab (b) Wave vector (c) Output efficiency	46

3.29 Hexagonal array PCS with bottom cladding (a=4 μ m; r=1 μ m) 48

3.30 Hybrid band structure of hexagonal array with bottom cladding 48

3.31 Square array of air holes PCS with bottom cladding 49

3.32 Hybrid Band structure of square array PCS with bottom cladding 49

3.33 Inband reflectance versus holes' depth 50

3.34 The temperature profile versus power 51

3.35 The increase of power supply voltage to maintain the fixed temperature as shutter in light path 52

3.36 The current-voltage curve of calculated and actual data 52

4.1 Standard MicraGEM fabrication process 58

4.2 Side view of our proposed device 61

4.3 Top view of our proposed device 61

4.4 The 3D models of two kinds of typical lattices arrays 62

4.5 The layout of the devices 64

4.6 TE PCB of square array with square holes (a=4.5um; w=2.5um; n=3.42) 65

4.7 TE PCB of square array with square holes (a=5um; width=3um; n=3.42) 65

4.8 Index distribution of the square array with square holes (Side view) 66

4.9 Simulation process of single cell 66

4.10 The simulation result of the proposed devices (wavelength monitor) 67

4.11 The relationship of wavelength and lattice for square lattice array With square air holes (w/a≈55%~60%) 68

4.12 The relationship of wavelength and lattice for hexagonal lattice array with circle air holes (d/a=1) 68

AI.1 FTIR with microscope 88

AII.1 The E and H field components are then interlaced in all three spatial dimensions 91

List of Tables

Table 4-1 Optimal geometry parameters 55

Table 4-2 Device diameters 64

List of Symbols

CH_4	methane
CO	carbon monoxide
CO_2	carbon dioxide
NO	nitrous oxide
SO_2	sulfur dioxide
Cr	chromium
Si	silicon
Ag	silver
Au	gold
ν	SP frequency
Γ	always denotes the origin k=0 of the Brillouin zone
k	the nearest neighbor direction of the Brillouin zone
$\vec{k}_0$	the wave vector of the incident radiation
$\vec{k}_{sp}$	SP wave vector
$\vec{k}_x$	Component of the incident wave vector (x direction)
$\vec{G}_x$	reciprocal lattice vectors (x axis)
$\vec{G}_y$	reciprocal lattice vectors (y axis)
Å	angstrom
μm	micron

ω frequency

ϵ_1 the dielectric constant of the interface medium

ϵ_2 the dielectric constant of the metal

λ wavelength

a lattice periodicity

c light speed

d diameter of holes

r radius of holes

θ incident angle

ϕ azimuthal angle

i, j integers

w width of square holes

List of Abbreviations

2D	two-dimension
3D	three-dimension
ATR	attenuated total reflectance
CMC	Canadian Microelectronics Corporation
DRIE	deep reactive ion etching
FDTD	finite difference time domain
FTIR	Fourier transforms infrared
FWHM	full-width half- maximum
IR	infrared
JPL	Jet Propulsion Laboratory
MEMS	micro-electro-mechanical systems
MicraGEM	Micralyne Generalized MEMS
PBC	periodic boundary condition
PBG	photonic band gap
PC	photonic crystal
PCS	photonic crystal slabs
PML	perfectly matched layer
PWM	plane wave method
SEM	Scanning Electron Microscope
SOI	Silicon on Isolator

SP	surface plasmon
SPR	surface plasmon resonance
TE	Transverse Electric
TM	Transverse Magnetic

CHAPTER I

INTRODUCTION

This chapter intends to overview the application of gas sensors, the development of conventional infrared gas sensors and novel micro-electro-mechanical systems (MEMS) infrared gas sensors, as well as to clarify the context arrangement of the research work in this thesis.

1.1 Overview

People have benefited a lot from using petrochemical products for heating, cooking, and transportation; however, ignition of these combustible products can have catastrophic effects. Gas sensors, which are used to monitor harmful gas to trigger alarm systems, have extensively utilized in industrial applications; for example, various manufacturing environments rely on early detection of toxic effluents, such as sulfur dioxide (SO_2), methane (CH_4), and nitrous oxide (NO), to ensure safe operation [1-3]. Recently, use of carbon monoxide (CO) gas detection for home safety and carbon dioxide (CO_2) sensing for building ventilation control has been continuously increasing [4]. Market analysis shows that gas sensors are expected to see the biggest growth of all sensor systems in the next decade.

Gas sensing has evolved to include technologies such as electrochemical, catalytic, semiconductor and infrared gas detection. Most sensor technologies would be classified as "reactive" that chemically interacts with the sensor element, providing an electrical signal that is proportional to the gas concentration [4]. These gas sensors have some

application for their inexpensive and lower power consumes. But these kinds of sensors are unreliable. They are unstable over time and temperature because of direct contact with other gases; it requires frequent calibration to reduce false alarms [1]

Infrared technology is "non-reactive", it does not chemically react with the gas since the sensor elements are sealed in vacuum and are not in contact with the gas. Thus, they are not poisoned by contact with the environment. Meanwhile, the infrared gas sensors have great reliability because IR gas sensors based on unique infrared absorption line provide conclusive identification and measurement of the target gas with little interference from other gases [1] [3] [5]. They have been theoretically and experimentally studied. People can measure the amount of absorbed infrared light to determine the gas concentration. Infrared gas sensors are reliable, accurate, and the measurement of choice for laboratory and industrial instruments, but they are not a choice for cost effective gas detection applications. Infrared sensors have not achieved appreciable penetration into mass markets because conventional IR gas sensors are expensive, high performance units for niche applications. Like computers in the early 1970's, they consist of a cabinet full of discrete components-often hand-selected and hand-assembled, are big, complex, and expensive. The IR gas sensors include a broadband IR Emitter, one or more IR detectors, each with a unique filter [1] [2] [5]. The mid-infrared optical quantum efficiencies are poor because of their lower bandgap energies. Thus, the broad, blackbody, "glowbar", hot filament sources remain as the primary means for IR light generation [6]. However, the IR sensors make up a significant part of the gas sensor instrument market, and IR

spectroscopy sensors remain the most accurate and reliable because they don't rely on catalytic or electrochemical interactions.

1.2 The novel MEMS infrared gas sensors

The novel optical-based gas sensors made on silicon wafers utilizing MEMS and surface textured technologies recently have attracted interest. All the optical components--emitter, filter, and detector – are built onto a single silicon chip, sealed in a vacuum and do not touch the gas [1-3]. The proposed infrared gas sensors combine the unique advantages of two different technologies: photonic crystal (PC) and surface plasmon (SP). PC consists of an array of holes etched into a dielectric substrate, and SP is a periodically perforated metallic thin film [7]. The thermal sources in the mid-infrared spectrum achieved by the surface modification (coupling to surface plasmon) to enhance the light extraction efficiency [6]. The novel unique thermally stimulated mid-infrared source emits radiation within a narrow range of wavelengths (spectral bandwidth of less than 10%) for sensing, spectroscopy and thermo photovoltaic applications [3] [6] [7]. The artificial surface texturing of silicon and metal thin film are fabricated onto a microbridge structure to enable power efficient heating of the device and to enhance its sensitivity to gas concentration. The proposed infrared gas sensors have wide application and a potential market for their small, accurate, reliable, lower power, and lower cost. The size of the integrated chip will be several square millimeters, and costs only a few dollars. The products will be used to detect toxic and combustible gases in homes, automobiles, public buildings and the work environment.

A photonic crystal is defined as periodically structured electromagnetic media (periodic dielectric constant), generally possessing Photonic Band Gaps (PBG) (analogous to the electronic bandgap present in semiconductors): ranges of frequency in which light cannot propagate through the structure [8-10]. When electromagnetic waves with the wavelength on the order of the period of the dielectric array propagate through this structure, the light interacts in a manner analogous to that for electrons in a periodic symmetric array of atoms [11]. The dielectric PC structures are passive and exhibit a strong absorption at resonance.

On top of the substrate there is an active periodically perforated metallic thin layer. The perforated metal film, where the apertures are on order of the wavelength of the light, permits resonant coupling of the incident radiation (from the underlying silicon) with surface plasmon (SP) at the metal surface [1-2]. The concept of SP originates in the plasma approach of Maxwell's theory [12]. The photons excite plasmons at the buried metal interface that couple with plasmons on the surface, which decay to release narrowband mid-IR radiation. The emission wavelengths are defined by a metal-coated silicon-air photonic crystal etched into the emitter surface. Upon heating, enhanced spontaneous thermal emission is observed from these photonic crystal modified surfaces presenting a unique technology for IR light generation [6]. This allows for tenability of the radiation and narrow emission at a designed wavelength. This technology promises a new class of tunable infrared emitter with high power in a narrow spectral band that are critical for sensing, spectroscopy, and thermo photovoltaic application [7]. An important

property of surface plasmons is the electromagnetic field enhancement at the interface compared with the incoming radiation. This enhancement can reach a factor of about 10 for a smooth flat surface, and even more for a rough surface. The transmission enhancement has been attributed to a resonance interaction of the incident radiation with SP polaritons at the metal surface. The interaction is made possible due to the grating coupling to the periodic surface structure. An alternative explanation for the high transmission efficiencies involves dynamical diffraction of light through the perforated metal film. [12-17].

The device works by electrically heating the micro-bridge, the emission process begins in the bulk silicon, where thermal stimulation produces blackbody-like radiation. When heated, the silicon acts like a hot filament and produces a wide spectrum of blackbody radiation. The PC reshapes this spectrum, centering it on the resonant wavelength defined by the lattice [1-2], but the device does not simply filter the blackbody emission. The photons cannot penetrate through the thin metal on the top surface. Instead, they excite surface plasmon modes at the lower substrate/gold interface, where vertical trenches create a boundary condition.

The proposed MEMS infrared gas sensors are built in photonic crystal and surface plasmon surface textured technologies and totally suspended single-crystal silicon micro-bridge structure with a high temperature coefficient of resistance. They emit and absorb maximally over a narrow band of wavelengths rather than over the whole blackbody spectrum, and maximize the sensitivity and signal-to-noise ratio of the sensors.

The exponential dependence of resistivity single-crystal silicon on the temperature in the "intrinsic" conduction regime enhances the signal-to-noise ratio of the detector considerably and enables the manufacture of a small, low-power, high- sensitivity gas sensor [18] [19].

1.3 Summary of the work

The proposed gas sensors and, in particular, the wavelength-selective emitter/detector components of the sensors are discussed as follow:

(1) The understanding of the interactions between electromagnetic radiation and textured solid surfaces

(2) The optimum designs and fabrication of MEMS surface textured optical devices.

The textures were designed according to the principles of photonic-band-gap (PBG) structures, which are characterized by spatially periodic variation of refractive index that gives to narrow "forbidden" wavelength transmission bands. The quantitative model to optimize the materials, geometry, and electrical properties of this suspended membrane MEMS Emitter/Detector are discussed in order to obtain high-power emission in a single, narrow spectral band mid-infrared gas sensor [7] [20] [21]. Meanwhile, the structure design is optimized, and a suitable fabrication technology for the proposed MEMS devices is proposed.

In optimizing pattern geometry, different models of the proposed devices are discussed, such as hexagonal lattice arrays with circle holes, square lattice arrays with

square holes, and square arrays with circle holes. Each structure has different lattice constant, the diameter and depth of holes. This concerns the relationship between the resonance wavelength of the narrow band emitter with the geometry structures and sizes: the lattice array and the depth of the air holes affect extractive efficiency of the devices [22-26]. Meanwhile, Band map and Gap map are helpful in optimizing photonic crystal design to achieve narrow bandgap in TE polarization with little interference from other gases. In the simulation of Photonic Crystal Slabs (PCS), a light line or light cone filter as a filter is employed to remove all of the radiation states from the band calculation. The modes of even or odd parallel the meaning of the TM and TE modes that are found in 2 D structures. In our proposed device, the air holes will extend into a certain depth of the silicon substrate. In this case, the light line is defined by the minimum of the light lines for both of side and bottom cladding [23] [24].

Finite Difference Time Domain (FDTD) [27-30] methods were used to do the simulation of the proposed devices, which include photonic crystal and surface plasmon structures. The main reason is that metallic materials in the crystal cannot be treated in the plane wave methods. The FDTD is a rigorous solution to Maxwell's equations. It is widely used as a propagation solution technique in integrated optics. It well predicts both the position and strengths of the absorption peaks. By changing the period of the surface photonic lattice, the SP peak and emissive band can be tuned to the designed wavelength. The boundary condition used the Perfectly Matched Layer (PML) implementation. Periodic boundary condition (PBC) is also chosen to analyze the periodic structures [27].

The simulation result of the wavelength monitor well express that the metallized surface 2 D photonic crystal of air holes in the silicon background yields a series of adequately spaced discrete peaks in the reflection spectrum, dominated by a single sharp feature corresponding to the lowest plasmon order [3]. However, the narrowest bandgap is not the only consideration; we also need to consider the extraction efficiency of the light and the fabrication technology process, such as the design rules of the technology files.

MEMS are highly miniaturized devices that integrate a number of functions including fluidics, optics, mechanics and electronics on a single silicon chip using techniques similar to traditional integrated circuit process technology. It merges sensing, actuating and computing into miniature systems that enable enhanced levels of perception, control and performance [31-33]. We use Silicon on Isolator (SOI) technology of MicraGEM (Micralyne Generalized MEMS) [26] to build the microbridge structure. MicraGEM is a MEMS prototyping process under development at Micralyne Incorporation in conjunction with the Canadian Microelectronics Corporation (CMC). This technology differs from traditional MEMS processes by the materials used in the process. This process enables user to develop fully suspended MEMS devices with metal electrodes (rather than silicon). We can theoretically design our proposed device in the range of tolerance without breaking the design rules. The released microstructures that consist of an array of holes etched into the silicon substrate, and surface plasmon modes in a metal-coated periodic lattice can achieve more precise and narrow wavelength selectivity. A simple lithographic mask change allows us to modify the spectral tuning of

the microbridge in production [1].

The measurements can be carried out on a Fourier Transform Infrared (FTIR) instrument; such as Nicolet Nexus 670 interferometer equipped with attenuated total reflectance (ATR) accessories. According to energy conservation, the absorption is $A=1-R-T \cong 1-R$, the transmission through the substrate is eliminated in the calculation since the transmission measurements showed that our samples are opaque to the radiation in infrared Emission and absorption of radiation are related processes. By Kirchoff's law, the emission of the structure is equal to the absorption under the same condition [7].

The thesis is divided into 5 chapters: the chapter 1 and 2, in which an overview of the development of gas sensors is made and the theoretical backgrounds are prepared for the surface textured MEMS infrared gas sensors. Chapter 3 and 4 introduce the optimization of the materials, geometry, and electrical properties of the proposed device; also design and fabrication of the device. Finally, Chapter5 covers conclusions and suggestions. Some suggestions for future works are proposed.

CHAPTEER II

THEORETICAL BACKGROUND

This chapter introduces the infrared absorption characters of common gases. It covers the theories of conventional infrared gas sensors and novel MEMS infrared gas sensors.

2.1 Infrared absorption characteristics of common gases

Infrared gas sensors are based on the fact that most gases have unique infrared absorption signatures in the 2-14 micron region [1] [3] [5] (showed in figure2.1), which is belong to the mid-infrared light region [4], as shown in figure 2.2. Optical gas sensors depend on measuring the transmission of light at a different wavelength for each gas. The particular wavelength identifies the gas and the amount of light absorbed by the gas determines the gas concentration [1] [2]. For example, the absorbed wavelength of SO_2 is 4 μm, CO_2 is 4.3 μm, CO is 4.7 μm, and NO is 5.3 μm. That means, when the infrared light generated from the emitter pass through the CO_2 gas, an infrared light with wavelength of 4.3 μm will be absorbed. We can measure the amount of absorbed infrared light to determine the CO_2 gas concentration. Thus, infrared gas sensors are excellent in term of accuracy and reliability on the measurement of the target gas with little interference from other gases.

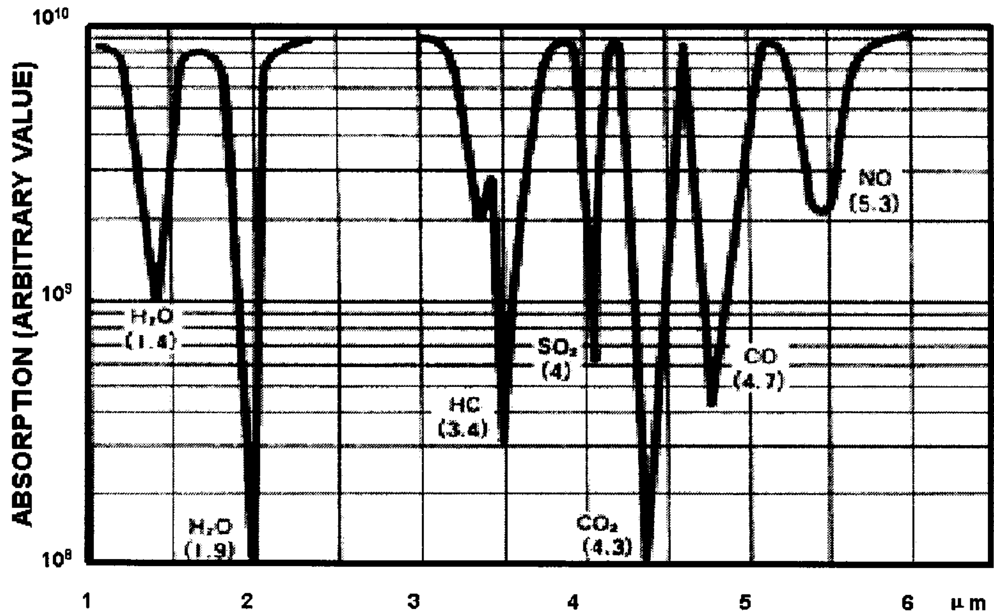

Figure 2.1 Infrared Absorption characteristics of Common Gases [1]

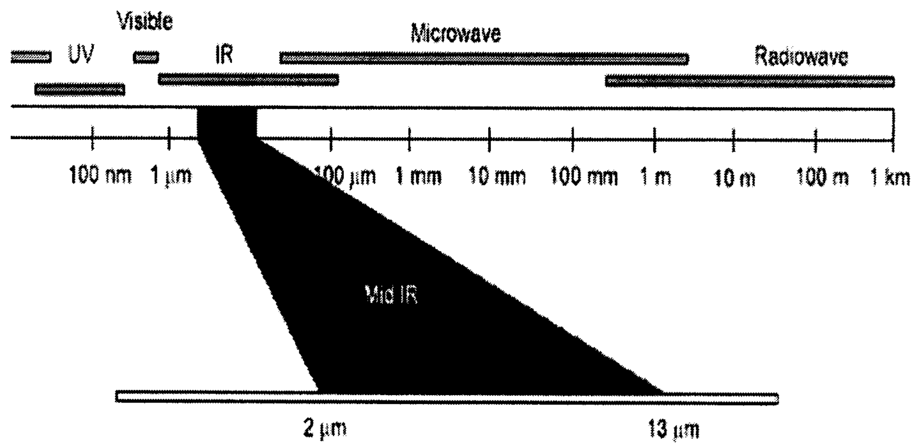

Figure 2.2 Distribution of light wavelengths [4]

2.2 The theory of conventional infrared gas sensor

Conventional infrared gas sensors, usually, include several discrete components: a broadband infrared light source (emitter), gas sample path, and one or more infrared detectors, each with an expensive optical filter [1] (showed in figure 2.3)

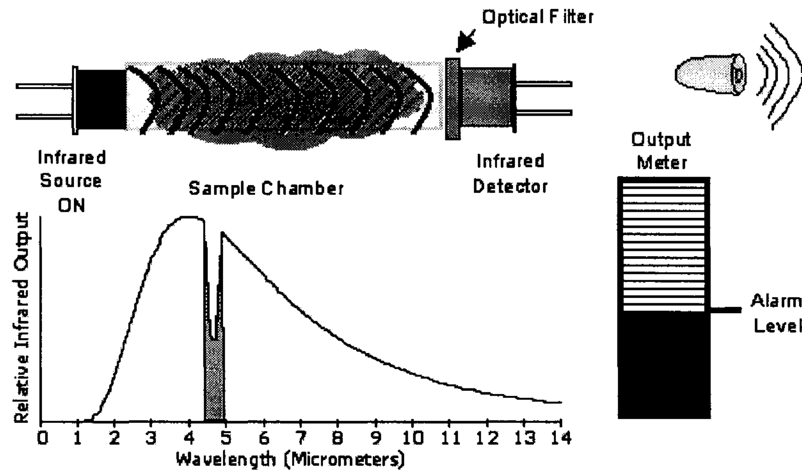

Figure 2.3 conventional infrared gas sensors [3]

The infrared emitter produces broadband (many wavelengths) infrared illumination. The optical filter restricts the view of the detector to a specific infrared wavelength for the target gas. The detector measures the amount of the specific infrared light. As the target gas enters the gas sample path, some of the infrared light that the wavelength correspondent with the target gas is absorbed (how much depends on the concentration of the target gas). This will cause the detector residing at a lower temperature. The drop in temperature will be measured via a change in resistance or voltage of detector, and trigger the audible alarm [1] [3].

From the above description, we can see that conventional gas sensors are big, complicated, and expensive since they are actually a cabinet full of several discrete components that are usually hand-selected and hand-assembled. However, these conventional infrared gas sensors remain the most accurate and reliable because they don't rely on catalytic or electrochemical interactions [3]. Thus, the infrared gas sensors make up a significant part of the gas sensor instrumentation market.

The main disadvantage of the kind of infrared gas sensor need a optical filter to filtrate the broadband infrared light that generated by the "glowbar" hot filament sources into a desired narrow band infrared light to the detector. If we have a desired unique narrow band mid-infrared light source, the problem will be solved. Although the new light sources in the visible and ultraviolet regions of the spectrum have rapidly developed, the generation of mid-infrared light has remained a challenge since the necessary bandgap energies are near those of thermal vibrations, and the optical quantum efficiencies in mid IR region are very poor [6]. In recent years, some people's works show that the thermal sources in the near and mid-infrared region may be enhanced through surface modification [34-37]. The novel infrared light sources that combine with photonic crystal and surface plasmon technologies have been developed. This coupling provides for unusually high optical transmission. The dielectric photonic crystal structure acts as a radiation reservoir for the conductive array, which in this case plays an active role through plasmon interactions. Meanwhile, the dielectric photonic crystal structure exhibits a strong absorption at resonance. It also services as a tuned infrared detector.

2.3 The theory of MEMS infrared gas sensors

The novel optical-based gas sensors made on silicon wafers utilizing MEMS technology has been experimentally and theoretically studied in Jet Propulsion Laboratory (JPL) of United States [1-3] [5-7]. The proposed MEMS infrared gas sensor (showed in figure 2.4), has recently triggered a lot of interest in connection with their

numerous potential technological applications. It uses MEMS fabrication technology to build all the optical components--emitter, filter, and detector -onto a single silicon chip. The chip employs the microbridge structures that enable power efficient heating of the device and enhance its sensitivity to gas concentration. By using photonic crystal and surface plasmon technology interaction, the device realizes the wavelength tuned into a unique narrow band infrared light source, and the light extrication efficiency has been greatly enhanced. The novel mid-infrared thermally stimulated narrow band emitter with a narrow waveband (a spectral bandwidth of less than 10%) centered on the signature wavelength of the target gas.

The device works by electrically heating the micro-bridge, which acts like a hot filament and produces a wide spectrum of blackbody radiation. The photonic crystal structures reshape the spectrum, centering it on the resonant wavelength for a particular gas. The chip, which serves as emitter, was then placed in a vacuum chamber and emits spectrally tuned infrared energy. The energy from the chip was shown out of the vacuum chamber through a sapphire window, travels along a short gas path and reflects off a gold- coated spherical mirror at the far-end of the sample chamber, focuses the light back through the gas and enter the sapphire window to the device, and is reabsorbed by the silicon micro-bridge that also serves as a tuned infrared detector. The micro-bridge is only sensitive to the light at the wavelength determined by its photonic bandgap pattern.

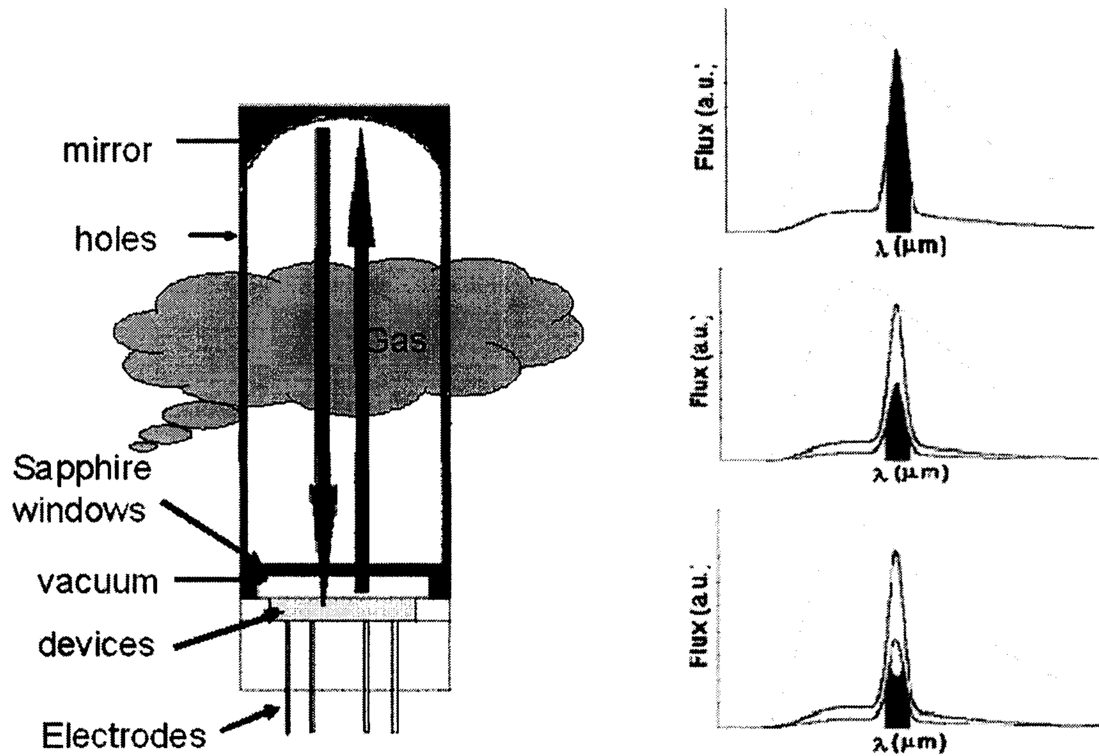

Figure 2.4 the theory of MEMS infrared gas sensors [1-2]

In this arrangement the silicon micro-bridge is receiving energy from both the electrical stimulation and reflected light and comes to thermal equilibrium. If the target gas is present, the gas absorbs some of the light and the light re-absorbed by the silicon micro-bridge will decrease, causing the system to reside at a lower temperature. The drop in temperature is proportional to the concentration of the target gas, and is measured via a change in resistance or voltage across the bridge.

In addition to the emitter/detector, the proposed sensor would contain a parabolic

reflector, a lens, and a mirror that would direct the infrared radiation along the desired optical path beginning and ending the emitter/detector [19].

From the analyses above, we found that the key of the proposed gas sensors is the surface modification technologies of the wavelength-selective emitter/detector components, which exploits the photonic crystal and surface plasmon technologies. Thus, the following description of the both theories will help to understand the interactions between electromagnetic radiations and textured solid surfaces.

2.4 The theories of photonic crystal and surface plasmon

2.4.1 Photonic crystal

Photonic crystals (PCs) are structures with a periodical dielectric constant. The performance of these synthesis crystals produces photonic bandgap (PBG), much as the crystal potential of semiconductor produces an electronic bandgap. Photons in the frequency range of band gap are completely excluded so that atoms within such materials are unable to spontaneously absorb and re-emit light in this region [14]. So, light cannot propagate through the structure [11] [19]. The dielectric photonic crystal structure is passive and exhibits a strong absorption at resonance. This acts as a radiation reservoir for conductive array. There has been considerable interest in investigating the unique optical properties of two- dimensional (2D) photonic crystals PCs. Corresponding to the polarization, there are two basic topologies for 2D photonic crystals, as depicted in Figure 2.5: high index rods surrounded by low index (left), and low-index holes in high

index (right). The important PBG characteristics are used to construct the narrow band Emitter/Detector.

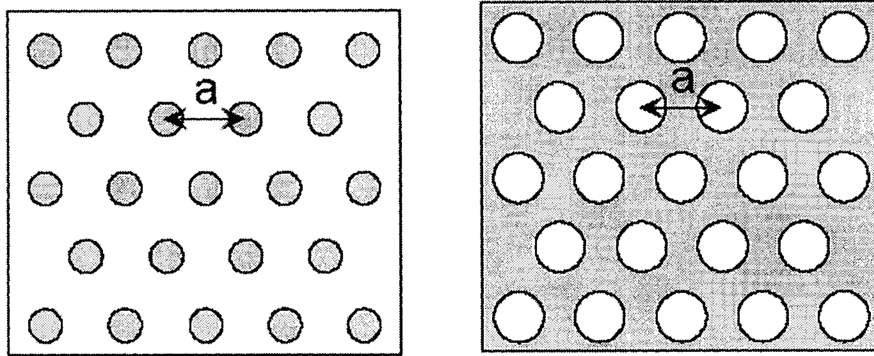

Figure 2.5 Two kinds of photonic crystals with a hexagonal lattice (rods/holes)

2.42 Surface plasmon

The concept of surface plasmons (SPs) originates in the plasma approach of Maxwell's theory: the free electrons of a metal are treated as an electron liquid of high density (plasma), and density fluctuations occurring on the surface of such a liquid are called plasmons, surface plasmons, or surface polarizations [12].

A surface plasmon (SP) is a collective excitation of the electrons at the interface between a conductor and an insulator. It is a charge density wave that occurs at an interface between a film and another medium. Plasmons are electromagnetic surface waves (we may think them as a ray of light) bound on a surface -propagating along the surface and present as an electromagnetic field. The field associated with the SP extends into the media adjacent to the interface and exponentially decaying away from it.

In our structures, optically thin metal film (gold) perforated with a periodic array

of air holes upon the PC silicon layer. The plasmon wave can be excited at the interface between gold and silicon layer. The silicon substrate is heated; the free carrier concentration in the silicon rises. With the photonic crystal patterning, the silicon substrate becomes a reservoir of photons at the resonant wavelength specifying to the array of PCs at its surface. The photons cannot penetrate through the thin metal on the top surface. Instead the photons excite surface plasmon modes at the low substrate/gold interface, where the vertical trenches create a boundary condition. There is a resonant interaction of the incident light with the surface plasmons on both surfaces of the metal film [1-2].

An important property of SPs is the electromagnetic field enhancement at the interface compared with the incoming radiation [13-17]. The transmission enhancement has been attributed to a resonant interaction of the incident radiation with SP polaritons at the metal surface. The interaction is made possible due to grating coupling to the periodic surface structure. This idea is supported by the observation that the surface plasmon dispersion relation measured from the enhanced transmission through large holes arrays with that predicted. Any periodic structure on the surface is sufficient to cause the transmission enhancement, even in the case of a single aperture surrounded by a periodic surface topography. The importance of surface plasmons is confirmed in numerical calculations on the interaction of light with a metal film with slits. An alternative explanation for the high transmission efficiencies involves dynamic diffraction of light. The transmission maxima are the result of a resonance excitation of SPs. Moreover, the

SPs on both sides of the metal film excited equally strongly by the incident light. This implies that the very high transmission efficiencies observed are related to an anomalously strong coupling of the SP modes on both sides of the metal film through the holes [16].

2.43 Surface Plasmon dispersion relation [3] [6] [13-17]

Since the wave vector of the plasmon wave is bound to the conductor surface, it is the wave-vector of the component of the incident light which is parallel to the conductor surface that can be equal to the wave-vector of the surface plasmons ($\vec{k}_{sp}, \vec{k}_x$ showed in Figure 2.6). The samples are defined to lie in (x, y) plane, the wave vector of incident radiation is $\vec{k}_0$, $|\vec{k}_0| = 2\pi/\lambda$; and the wave vector of the incident radiation in the $\vec{k}_x$ direction: $\vec{k}_x = \vec{k}_0 \sin\theta = 2\pi \sin\theta / \lambda$

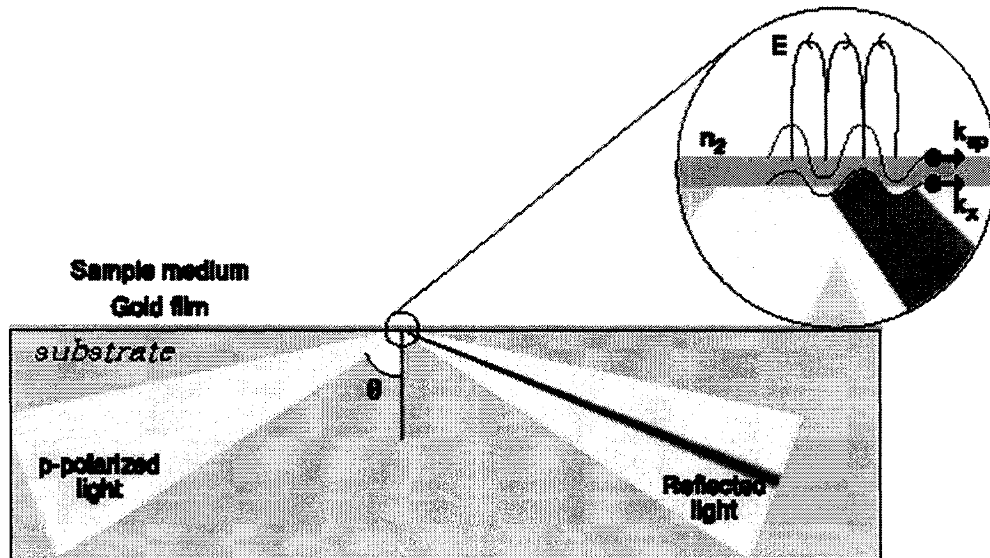

Figure 2.6 Surface plasmon resonance (SPR) is excited by p-polarized totally internally reflected light at a silicon /metal film interface, the surface plasmon enhancing the evanescent field amplitude, E [15].

According to the result from a resonance interaction of the incident light with SPs on both surfaces of the metal film, the interaction is made by coupling through the grating momentum and obeys conservation of momentum:

$$\vec{k}_{sp} = \vec{k}_x \pm i\vec{G}_x \pm j\vec{G}_y \qquad 2\text{-}1$$

Where $\vec{k}_{sp}$ is the surface plasmon wave vector, $\vec{k}_x$ is the component of the incident wave vector that lies in the plane of the sample as defined above. $\vec{G}_x$ and $\vec{G}_y$ are reciprocal lattice vectors. The SP dispersion relation is as follow:

$$\left|\vec{k}_{sp}\right| = \frac{\omega}{c}\left[\frac{\epsilon_1\epsilon_2}{\epsilon_1 + \epsilon_2}\right]^{1/2} \qquad 2\text{-}2$$

Here ω is the angle frequency of radiation, ϵ_1 is the dielectric constant of the interface medium, and ϵ_2 is that of the metal.

Surface plasmon dispersion of square lattice array:

The frequencies of the SP modes are obtained by combining Equation (2-1) and (2-2) to obtain:

$$\left(\frac{\omega}{c}\right)^2\left(\frac{\epsilon_1\epsilon_2}{\epsilon_1 + \epsilon_2}\right) = \left(\frac{\omega}{c}\right)^2\left[\left(\sin\theta\cos\phi \pm \frac{iG_x}{\omega/c}\right)^2 + \left(\sin\theta\sin\phi \pm \frac{jG_y}{\omega/c}\right)^2\right] \qquad 2\text{-}3$$

Which is solved for different integers i, j in the reciprocal square lattice (ϕ is the azimuthal angle). $\left|\vec{G}_x\right| = \left|\vec{G}_y\right| = 2\pi/a_0$, and i, j are integers. At normal incidence $\theta=0$, and equation (2-1) and (2-2) reduce to

$$(i^2 + j^2)^{1/2}\lambda = a_0\left[\frac{\in_1\in_2}{\in_1 + \in 2}\right]^{1/2} \qquad 2\text{-}4$$

For normal incidence, the lowest frequency SP has a wavelength nearly equal to the lattice period of the grating.

Surface plasmon dispersion of Hexagonal lattice array [3]:

The corresponding reciprocal lattice vectors are: $G_1 = \frac{2\pi}{a}\left(1, -\frac{1}{\sqrt{3}}\right), G_2 = \frac{2\pi}{a}\left(0, \frac{2}{\sqrt{3}}\right)$,

and the eigenvalue equation for the SP frequencies will be:

$$\left[\frac{\in_1\in_2}{\in_1 + \in_2}\right] = \left[\sin\theta\cos\phi \pm i\frac{\nu_0}{\nu}\right]^2 + \left[\sin\theta\sin\phi \mp i\frac{1}{\sqrt{3}}\frac{\nu_0}{\nu} \pm j\frac{2}{\sqrt{3}}\frac{\nu_0}{\nu}\right]^2 \qquad 2\text{-}5$$

Here, ν is SP frequency, i and j are integers, ϕ is the azimuthal angle, and $\nu_0 = c/a$. The fundamental SP mode (i=1, j=0 or i=0, j=1, corresponding to the first shell of G vectors) occurs at a wavelength of $\sqrt{3}a/2$. The wavelengths decrease with increasing shell of G vectors.

From the equations 2-4 and 2-5, it results that the dielectric layer in contact with the metal along with the lattice constant of the array will influence the position of the resonant wavelength. Figure 2.7 is the simulation and measurement results of square arrays with square holes [6]. Figure 2.8 shows the simulation result of hexagonal lattice arrays with circle holes (a=3 and 4 μm) [3]. The results show a series of adequately spaced discrete peaks in the reflection spectrum, dominated by a single sharp feature corresponding to the lowest plasmon order, in an otherwise uniform highly reflective (>90%) over most of the IR spectrum. This, in turn, gives rise to a sharp absorption

feature with a correspondingly narrow thermal emission peak in the emission spectrum. The simple plasmon theory predicts the location of the SP modes very well.

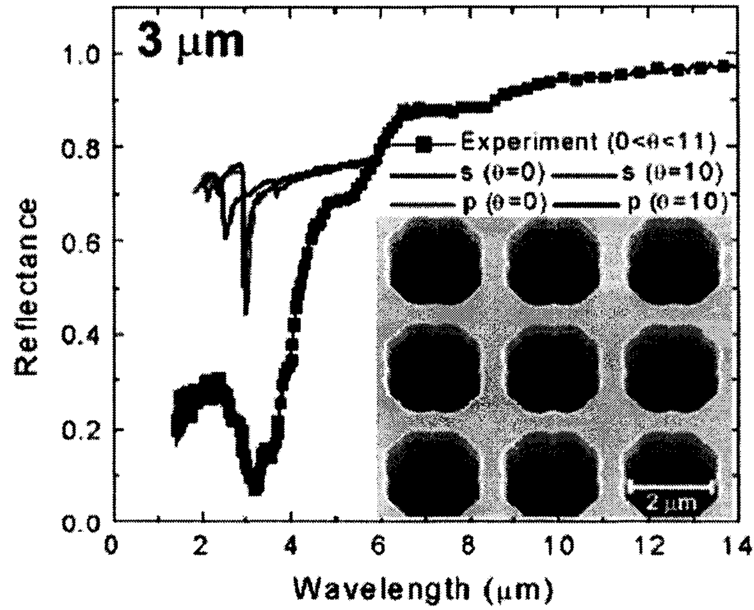

Figure 2.7 The simulation and measurement results of square arrays with square holes [6]

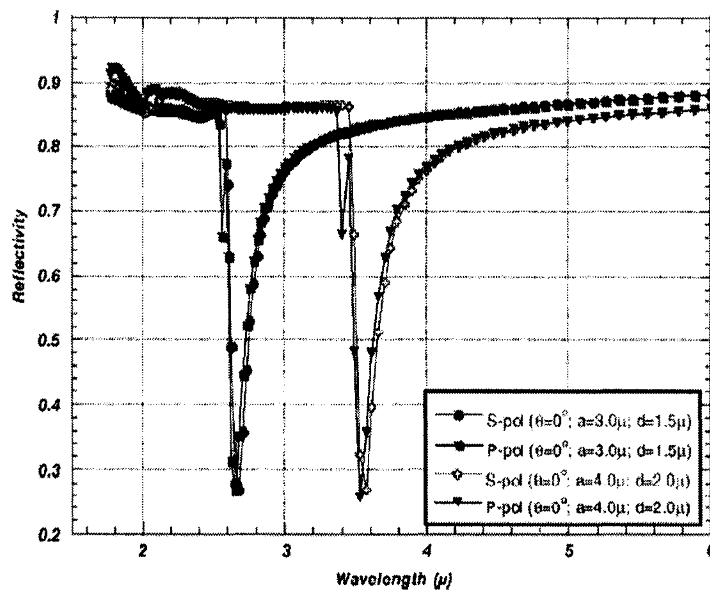

Figure 2.8 The simulation of reflectivity with different hexagonal lattice arrays of circle holes [3]

CHAPTER III

OPTIMAL MATERIALS, GEOMETRIES, AND ELECTRICAL PROPERTIES FOR PROPOSED DEVICES

From the discussion above, we know that metallized 2 D photonic crystals structures, which serve as infrared Emitter/Detector, can generate narrow band infrared light with high transmission efficiency. To achieve this performance, we need to optimize the materials, geometry, and electrical properties of the proposed device combining with the fabrication technology process.

3.1 materials

Firstly, we consider the material of the metal film that perforated with a periodic array of air holes. The collective's excitations of electron density lead to the formation of surface plasmon (SP) polarizations. From the transmission properties, the material of the metal layer that perforated with air hole arrays express similar properties in Au, Ag, and Cr. The important thing is the film must be metallic, nonmetallic materials have small transmission efficiencies at all wavelengths. Usually, gold (Au) is a preferred metal as its good electrical, mechanical and chemical properties: serve as electrodes, mirror- smooth membranes, and anti-corrosion. Many MEMS processing use Au as the metal layers. Mathematically, electromagnetic fields associated with the plasmon can be found from Maxwell's equations if the dielectric response of the media is lumped into corresponding complex dielectric constants. For the solution to exist, the dielectric constants should satisfy several conditions:

-The dielectric constant of the metal should be real and positive;

-The real part of the metal dielectric constant must be negative and its absolute value should be greater than the imaginary part.

Giving an example: default values for an average gold layer should be something like: e`=-12.xxx, e``=1.5xx and the thickness in the range of 450-500Å. The metal dielectric constant's imaginary part determines how fast the plasmons decay by dissipating their energy into heat. Therefore one wishes to have it small, obtaining a nice sharp plasmon curve with a minimum close to zero %of reflected light.

Next is the photonic crystal material. Usually, only nonmetallic materials are used for the fabrication of PCs operating in the spectral range of a material transparency. From the SP dispersion relation, we know that the resonance states are dependent upon three factors: the lattice periodicity, the dielectric properties of the material below the metal, and the depth of the air holes in the photonic lattice. Some people did the research work that fabricated the arrays on silicon; silicon dioxide and silicon nitride substrates using MEMS- based processing methods [7]. They found the dielectric influences the position of the resonance as well as the width of the emission.

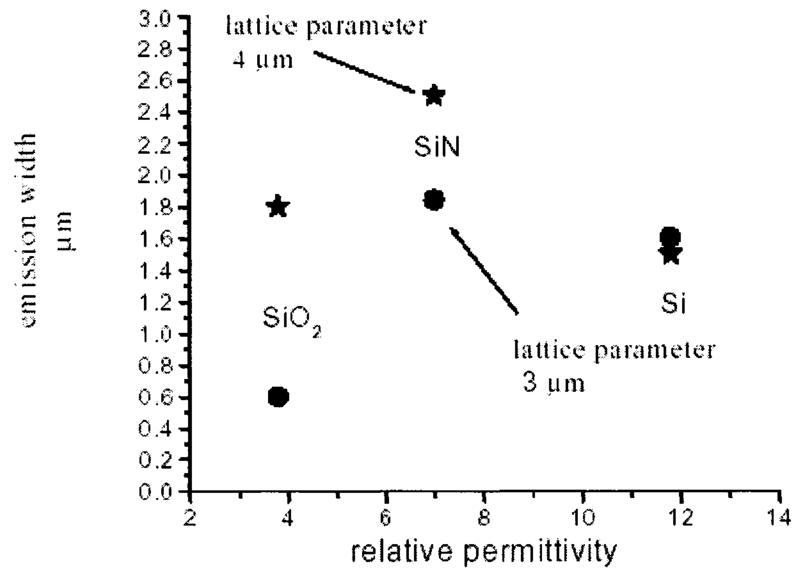

Figure 3.1 Dielectric influence on the width of the emission (square lattices) [7]

In Figure 3.1, SiN appears to be the worse for applications: the widths of emission are 2.5 μm (a= 4 μm) and1.9 μm (a=3 μm). SiO2 exhibits big different emission width: 1.8 μm (a= 4 μm) and 0.6 (a=3 μm). Silicon appears good and has stable characteristics of the narrow emission width: 1.6 μm (a=3, 4 μm). It should be a good choice for narrow band Emitter. Silicon has an exponential dependence of resistivity on temperature in the "intrinsic" conduction regime and this is another advantage that this material has compared to others. At high temperatures, the rate of carrier generation in silicon becomes high, so that the amount of mobile carriers (n0 and p0) exceeds the impurity concentration (Donor or Acceptor) .This effect enhances the signal to noise ratio of the device considerably and enables the manufacture of a small, low- power, high sensitivity gas sensor [7] [19]. Also silicon is used in many technologies to fabricate MEMS.

Conclusion: From the discussion above, we found that silicon is desired material to perform photonic crystal structure and gold for surface plasmons.

3.2 optimization of geometry of the proposed device

We have known that the "bar" structure (high index rods surrounded by low index) and the "holes" structure (low-index holes in high index) are typical 2D photonic crystal structures, which produce photonic bandgaps (PBG). The "bar" photonic crystal structures are suitable to the outside light source passes through it and generates the photonic bandgaps, as show on Figure 3.2.

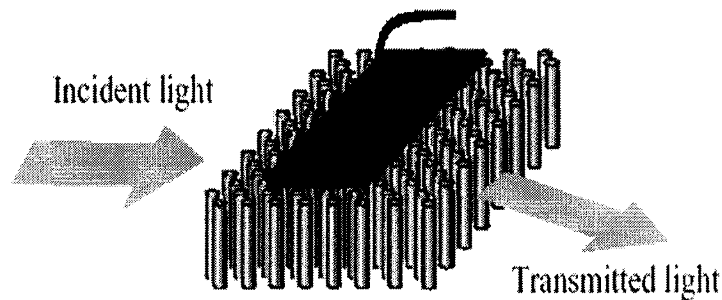

Figure 3.2 Light propagate in "Bar" structure photonic crystal

The proposed device can generate broadband infrared light in bulk silicon by electrical heating. The holes in the PC structure reshape the spectrum into a narrow band IR with desired wavelength. From the point of view of hole lattice array, the lattice types are divided into hexagonal and square arrays. Three different structures were studied; hexagonal arrays with circle holes, square array with circle holes, and square array with square holes. The light propagation characteristics in these structures were analyzed theoretically and experimentally. Figure 3.3 shows hexagonal array with circle holes (a), square array with circle holes (b), and square arrays with square holes (c).

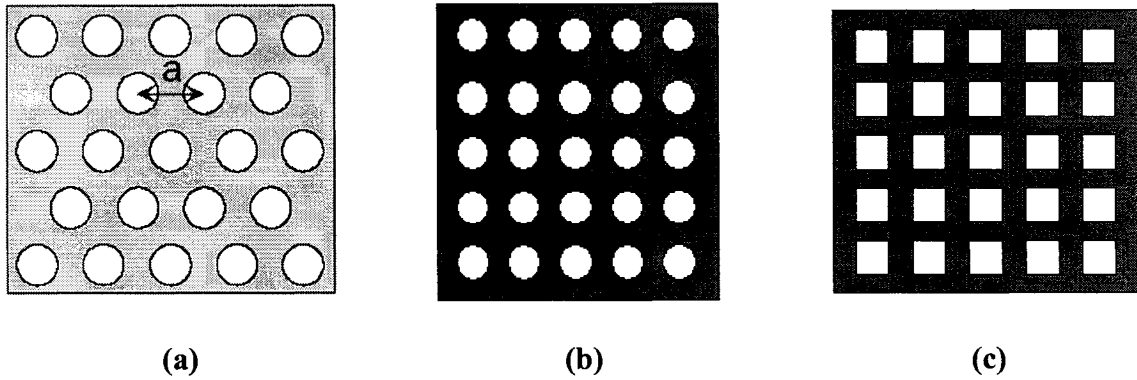

Figure 3.3 (a) hexagonal array with circle holes, (b) square array with circle holes, and (c) square array with square holes (c)

3.2.1 The definition of the polarizations:

The fields in 2D can be divided into two polarizations by symmetry: TM (transverse magnetic), in which the magnetic field is in the plane and the electric field is in perpendicular direction; and TE (transverse electric), in which the electric fields in the plane and the magnetic field is in perpendicular direction. Recall that a PBG requires that the electric field lines run along thin veins; thus, the air holes in the dielectric structure is best suited for TE light (TE running around the holes).

3.2.2 Photonic bandgaps

In this section, the relationship between the bandgaps with geometry of the three lattice arrays is discussed. The plane wave method (PWM) is used to do the simulation of photonic bandgaps; it is faster, more accurate and allows it to automatically identify band gaps. Even if we will ultimately use the FDTD method [27], which will discuss later, we should always perform preliminary calculations with the plane wave method to establish the basic behavior.

Firstly, we build a hexagonal lattice (showed in Figure 3.4) as an example:

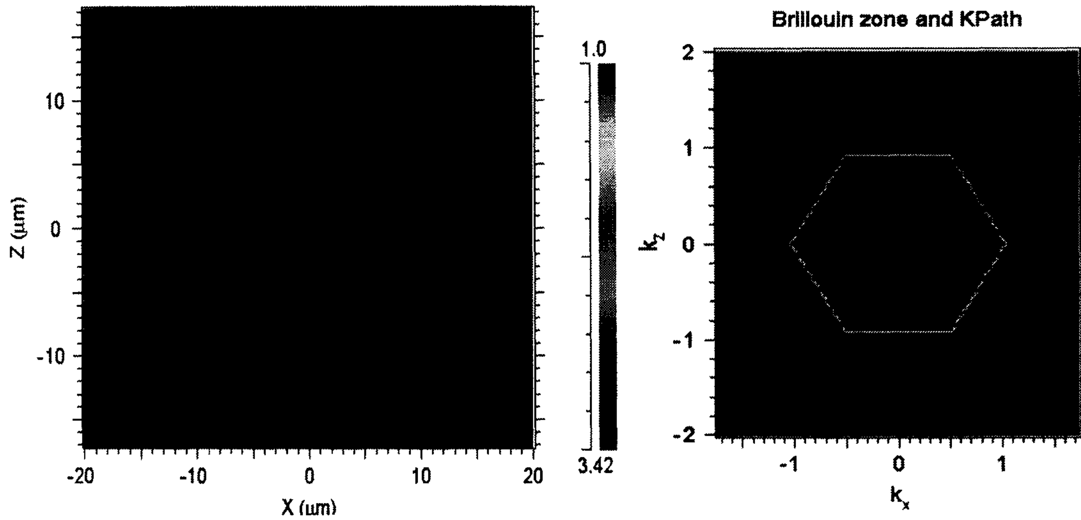

Figure 3.4 hexagonal lattices with air holes. **Figure 3.5** Brillouin zone and Kpath

--The first Brillouin Zone [24]**:**

When we study the optical modes of conventional photonic structures, we have to solve the problem in the neighborhood of the origin of reciprocal or wave vector space. To make this neighborhood precise, that defines the First Brillouin Zone (FBZ or 1BZ): The First Brillouin Zone of reciprocal space consists of all points closer to the origin than to any other reciprocal lattice vector. Each crystal structure is characterized by a set of symmetry points denoted by more or less standard letters. To construct a band diagram, we identify the symmetry points of the 1BZ and connect them by straight lines.

Figure 3.5 shows the Brillouin zone of a hexagonal lattice, with the irreducible Brillouin zone (follow the six fold symmetry of the crystal); the corners (high symmetry points) of this zone are given canonical names, where r always denotes the origin k=0, k is the nearest neighbor direction. In practice, the band extremes almost always occur

along the boundaries of the irreducible zone (such as the high-symmetry directions). So it is conventional to plot the bands only along these zone boundaries in order to identify the band gap.

Figure 3.6 shows the TE band gaps of a hexagonal lattice with r=0.25a, where the lattice constant is a, and r is the radius of holes. We can see that when the diameter of the holes is about half of the lattice constant, TE PBG has a bandgap in the range of 0.2~0.24 frequency, and a narrower bandgap in the range of 0.55~0.56 frequency. Photons in the range of frequency of bandgap cannot propagate along structure can; therefore the spontaneously absorption or emission is not possible [14].

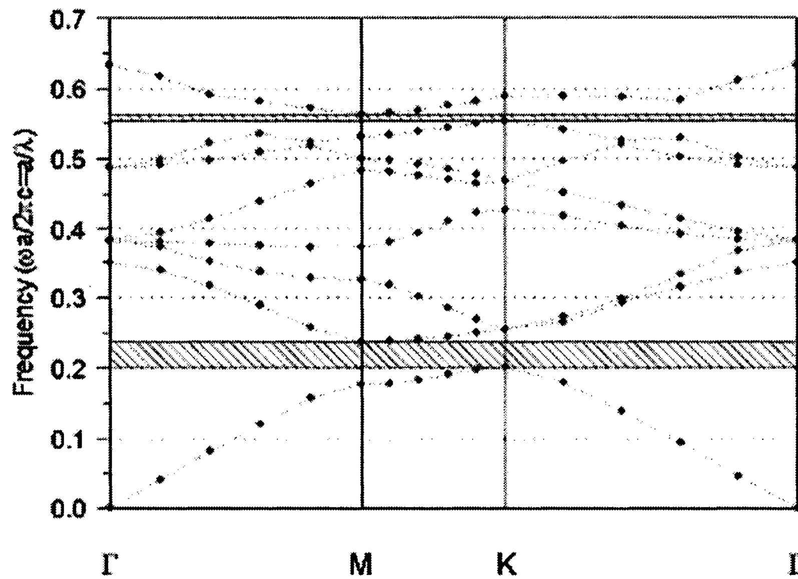

Figure 3.6 TE PBG for hexagonal lattices of air holes (r=0.25a)

Figure 3.7 shows the TM PBG for hexagonal lattices of air holes. In this structure, there is no bandgap in the TM diagram.

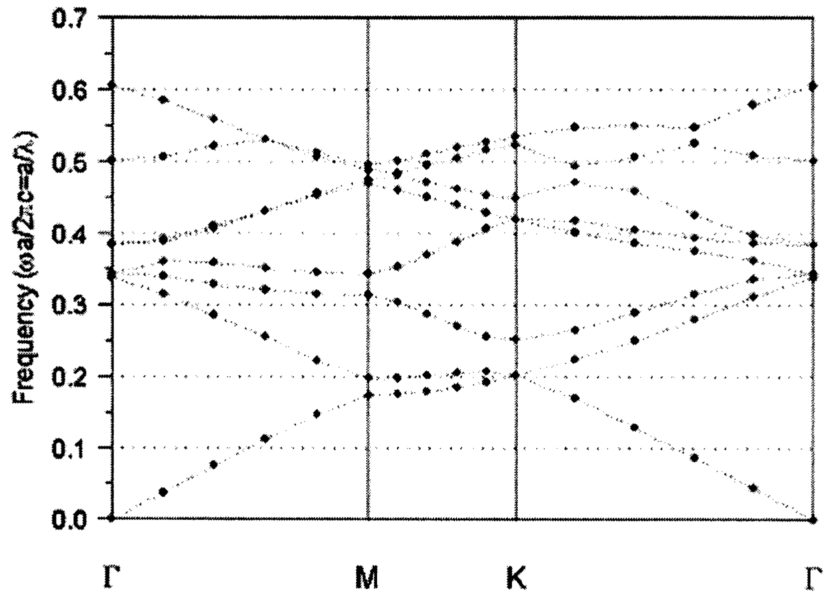

Figure 3.7 TM PBG for hexagonal lattices of air holes (r=0.25a)

Now, we change the radius of air holes, such as r=0.3a, to get new TE PBG for hexagonal lattices of air holes (showed in Figure 3.8). We find that there are two wide band gaps in the TE BGP diagram: in the range of 0.21 ~0.275 and 0.59~ 0.62 frequencies and they are wider than of the case (r=0.25a). Figure 3.9 shows the TM PBG for hexagonal lattices of air holes(r=0.3a). In this structure, there is also no bandgap in the TM*PBG diagram.

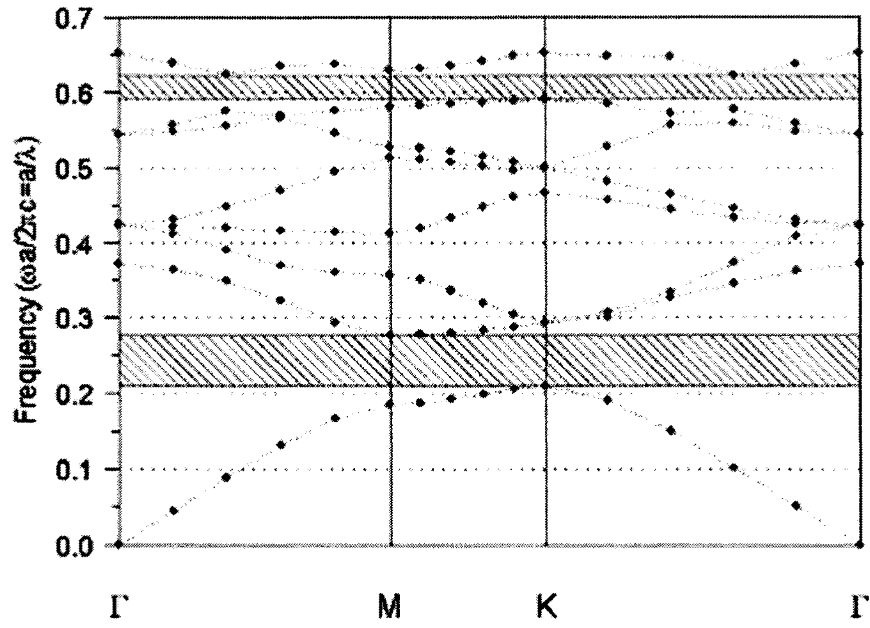

Figure 3.8 TE PBG for hexagonal lattices of air holes (r=0.3a)

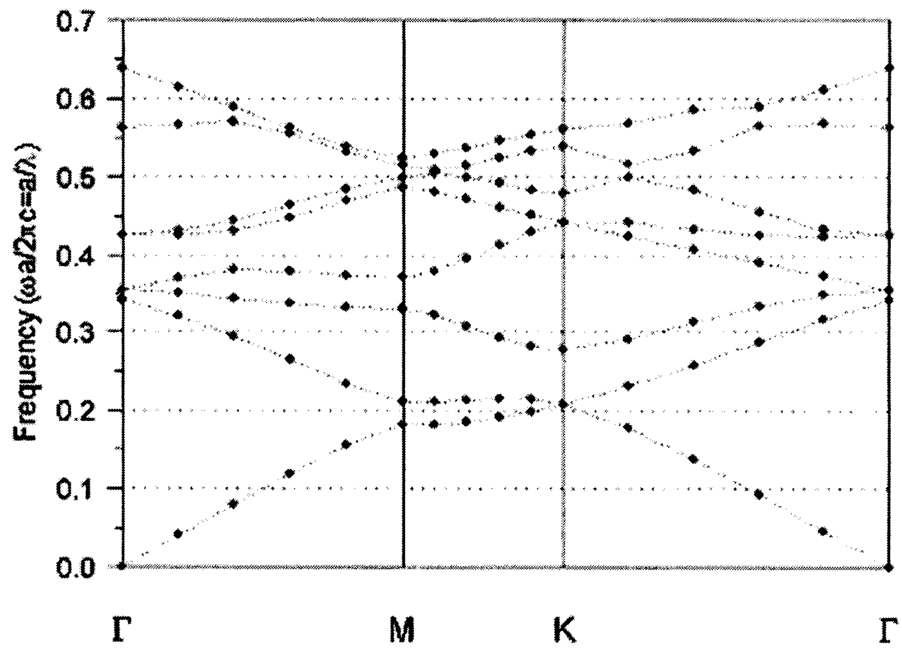

Figure 3.9 TM PBG for hexagonal lattices of air holes (r=0.3a)

Next, we present the simulation results of the square arrays with circles holes.

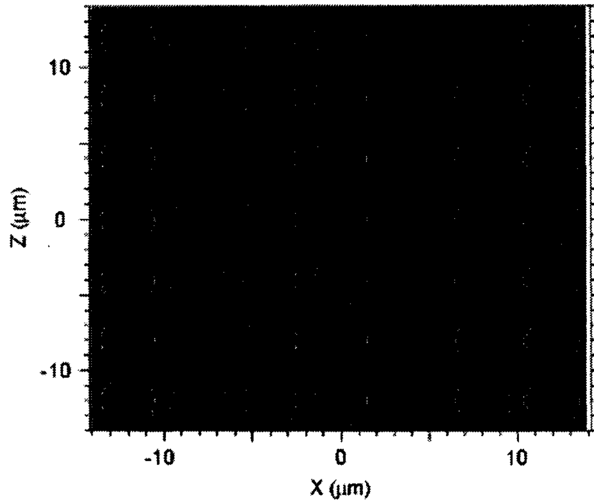

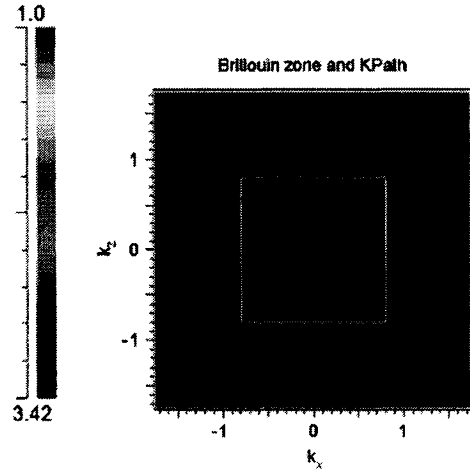

Figure 3.10 square arrays with circle air holes **Figure 3.11** Brillouin zone and K path

Figure 3.10 shows the dielectric distribution of the square arrays with circle air holes in silicon substrate, which its reflective constant is 3.42. Figure 3.11 is the Brillouin zone (follow the four fold symmetry of the crystal) and k path of the square arrays.

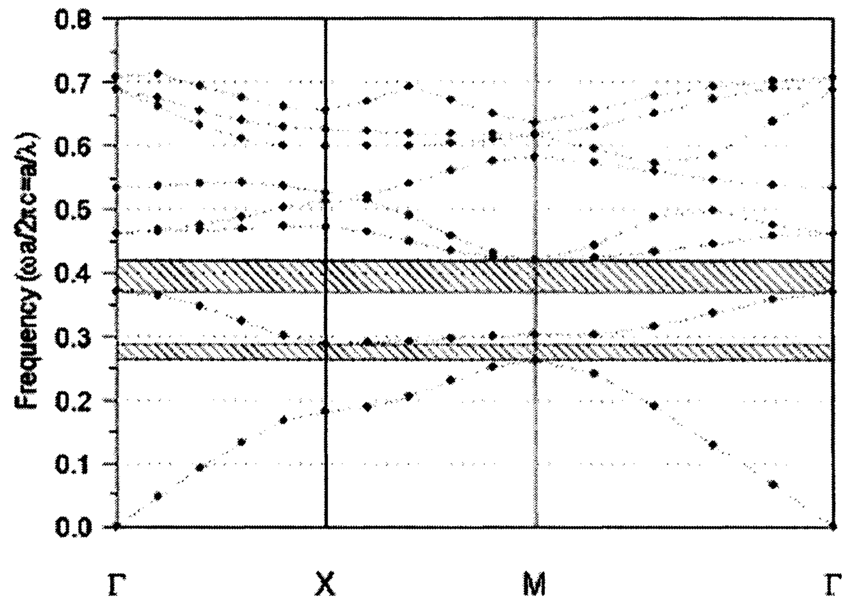

Figure 3.12 TE PBG of square arrays with circle air holes (r=0.4a)

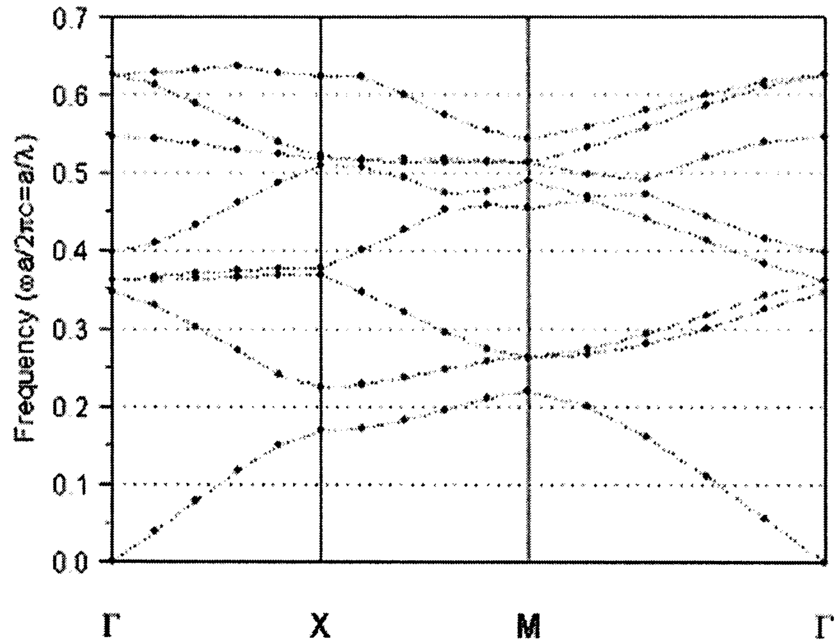

Figure 3.13 TM PBG of square arrays with circle air holes (r=0.4a)

Figure 3.12 shows the TE PBG of square arrays with circle air holes, which the diameter of air holes is 80% of the lattice. We find there are two band gaps: in the ranges of 0.26 ~ 0.29 and 0.37 ~ 0.42 frequencies. Figure 3.13 shows the TM PBG of square arrays with circle air holes (r=0.4a). There is no TM band gap.

Now, we change the radius of air holes; for example, r=0.28a, we do the simulation of the square arrays with circle air holes in silicon substrate. Figure 3.14 shows its TE PBG and Figure 3.15 shows it's TM PBG diagram. There are no band gaps in both PBG diagram.

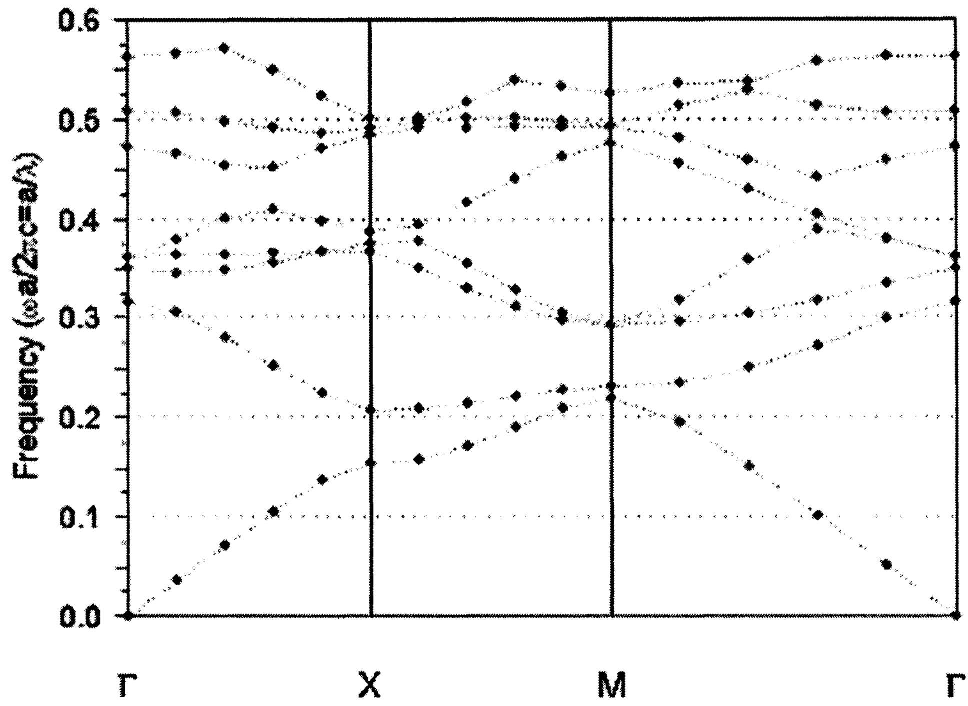

Figure 3.14 TE PBG of square arrays with circle holes (r=0.28a)

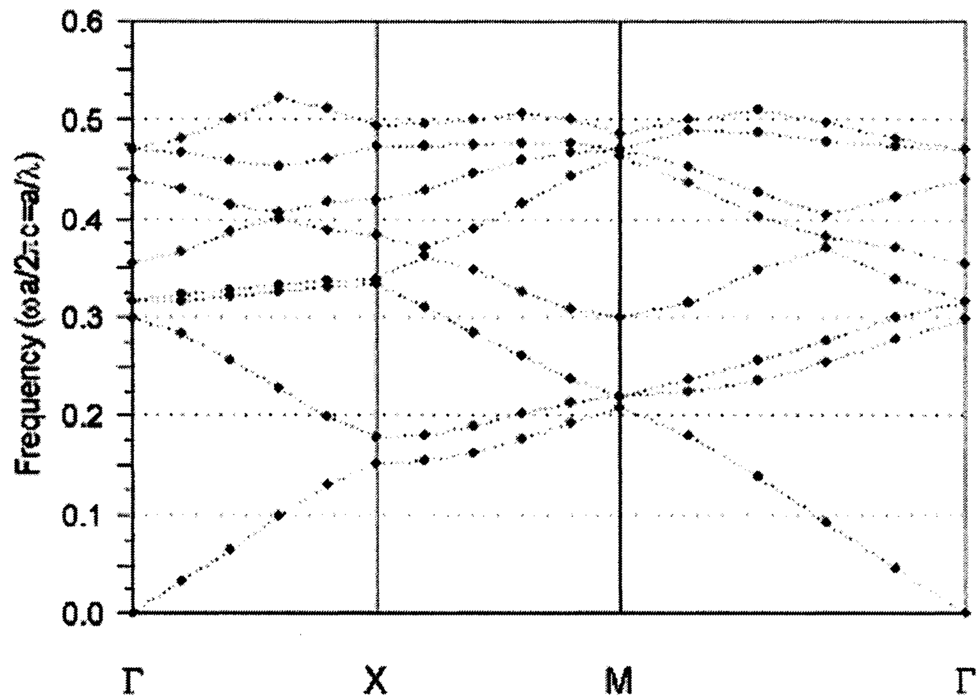

Figure 3.15 TM PBG of square with circle holes (r=0.28a)

Finally, we present the simulation result of square arrays with square air holes.

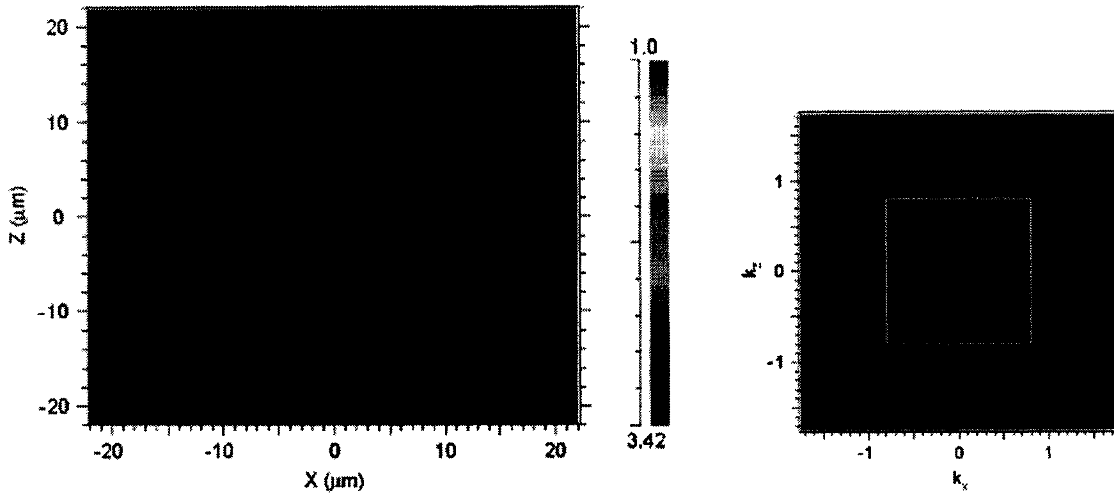

Figure 3.16 square arrays with square holes **Figure 3.17** Brillouin zone of square Array

Figure 3.16 shows the distribution of square array with square air holes in silicon (n=3.42) substrate, and Figure 3.17 is its Brillouin zone. Figure 3.18 is TE PBG of square arrays with square air holes in silicon substrate; the width of the air holes is 60% of lattice. There is a bandgap in the range of 0.24~0.26 frequency. Fig. 3.19 is its TM PBG diagram. There is no band gap in it.

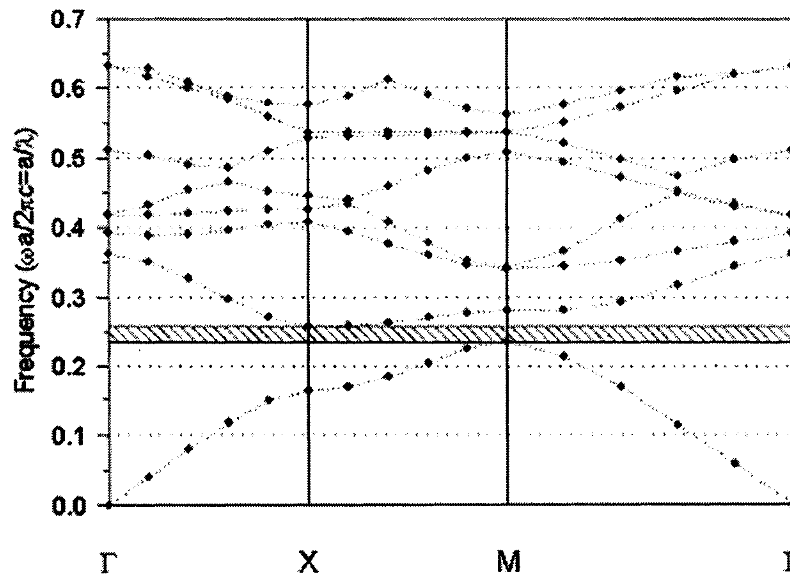

Figure 3.18 TE PBG of square arrays with square air holes (w=0.6a)

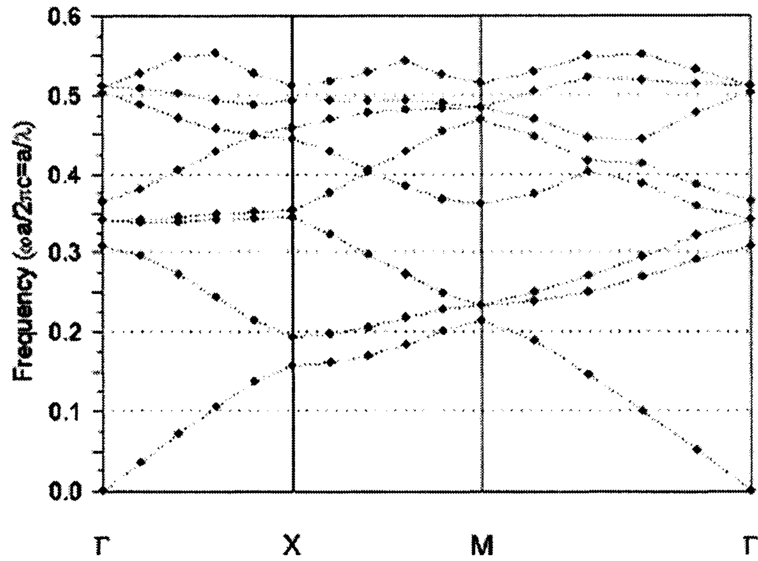

Figure 3.19 TM PBG of square arrays with square air holes (w=0.6a)

We also can change the width of air holes in lattices. Figure 3.20 is TE PBG of square arrays with square air holes (w=0.75a), and Figure 3.21 is the case of w=0.56a. There are no bandgaps of TM PBG in both cases.

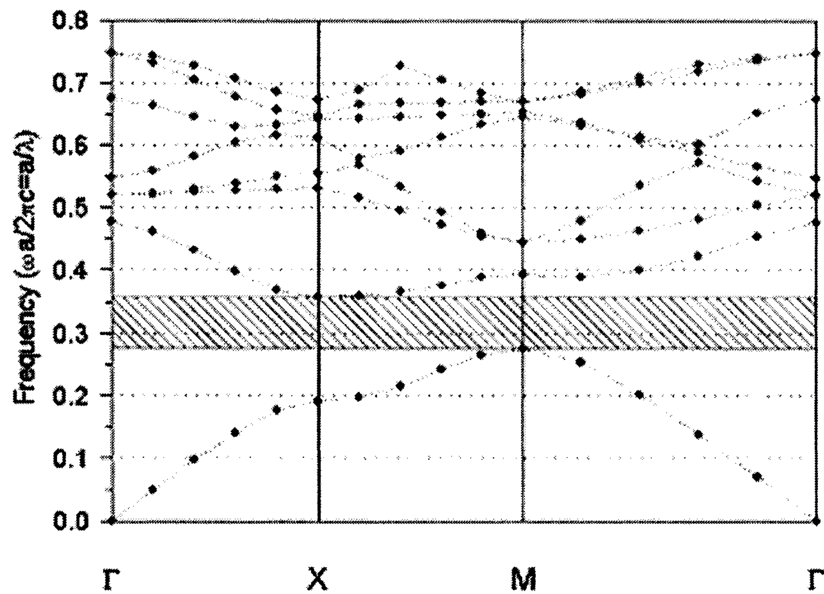

Figure 3.20 TE PBG of square arrays with square air holes (w=0.75a)

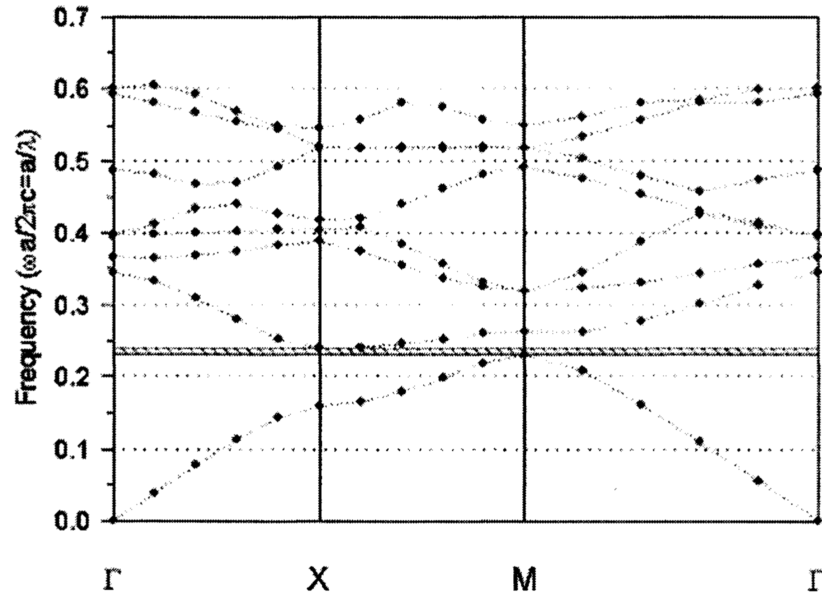

Figure 3.21 TE PBG of square arrays with square air holes (w=0.56a)

Conclusion:

From the TE and TM PBG of three kinds of lattice arrays: hexagonal arrays with circle air holes, square arrays with circle and square air holes in silicon substrates, we found that the TE PBGs will become wider with increasing the ratio of diameter (for hexagonal array with circle holes) or side (for square array with square holes) to air hole lattice constant. Optimizing design deals with how to define the sizes of air holes to get the desired structure for proposed photonic devices. For hexagonal arrays, we found that the diameter of air holes is near half of the lattice constant, the structure can generate a desire bandgap for the proposed device. For the square arrays with circle air holes, only the air holes with large diameter (70% of lattice) can achieve bandgaps. For the square arrays with square air holes, the width of the air holes between 55% and 60% is desired

value for the proposed device.

3.2.3 Optimizing Band gap:

For most real applications, performing a single band structure calculation is insufficient. In order to create a workable structure, a designer needs to identify important parameters and optimize their values to achieve the desired results. A related problem is to evaluate the acceptable tolerances in design parameters.

In optimizing photonic crystal designs, it is frequently important to characterize the band structure as a function of one or more design parameters. If the main interest is in optimizing gaps, then band diagrams such as those in Figure 3.6 carry more information than is needed, we don't need to know the particular symmetry points at which the band edges occur; we just need to know whether or not a gap exists throughout the 1BZ and if there is what its bandwidth is. By compressing the plot horizontally to a single point, we can represent the band structure as a series of vertical lines-a reduced band structure. The gaps appear as the spaces between the lines. We can then vary a design parameter, and observe how the distribution of gaps and bands changes.

Figure 3.22 (upper part) should make this idea clear. The reduced band structure for the 2D hexagonal lattice is shown as a function of the radius of the holes. Figure 3.22 (lower part) shows the gap map for the same problem, which is just the inverse of the reduced band structure. The gap map indicates that TM gap exists over a much wider range compare to that of TE gap. It is also easy to identify the optimum radius for a joint gap.

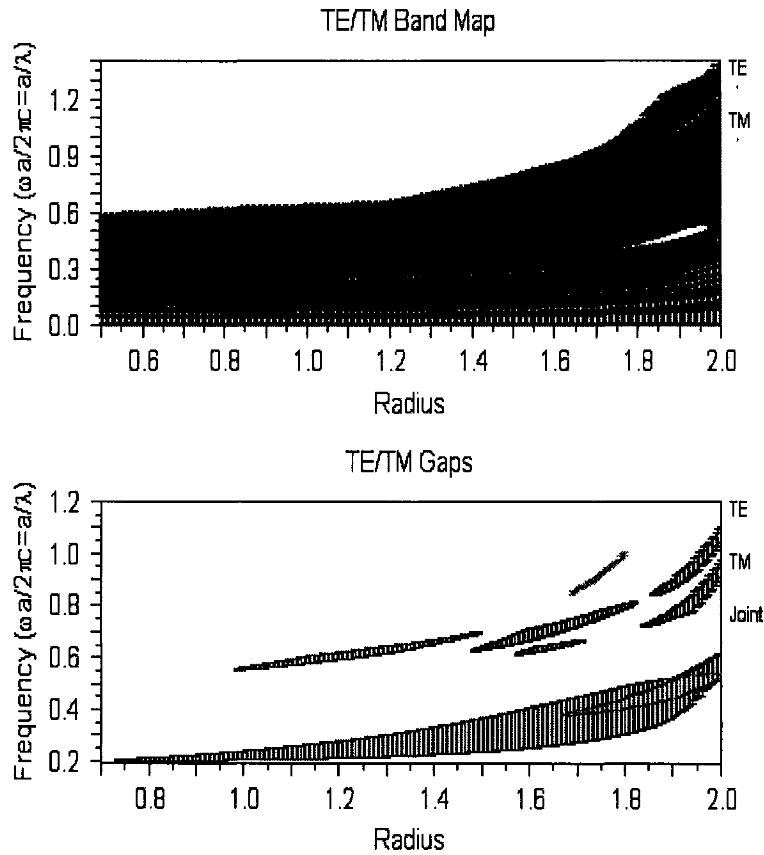

Figure 3.22 TE/TM Band Map and Gaps of hexagonal lattice with air holes

Band map [24]

The band map in the upper part of Fig.3.22 contains a point for every mode calculated in the entire scan. As each band structure is completed, all the frequency eigenvalue from the entire k-path are combined and plotted in the band map along a single vertical line corresponding to the current value of the scanned variable. Thus in Fig. 3.22, we see how the bands move as the radius varies. Vertical bars with horizontal caps also indicate the range of each band. In this case, we defined the lattice constant as 4 micron, the radius of air holes change from 0.5 to 2 micron, and in step of 0.01micron.

Gap map [24]

For the current problem, the lower gap map is perhaps easier to interpret. For each value of the Radius, vertical bars indicate all the gaps that were found. This is useful from a design perspective because one can find the gaps that correspond to various physical design values.

Similarly, Figure 3.23 shows TE/TM Band Map and Gaps of square array with circle air holes, and Figure 3.24 is the same case for the square array with square air holes.

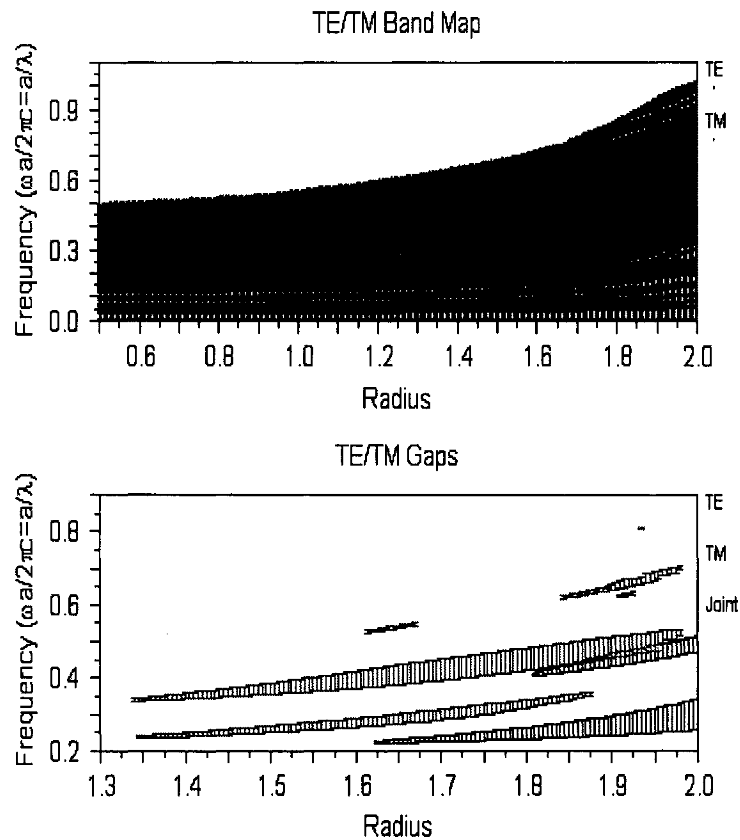

Figure 3.23 TE/TM Band Map and Gaps of square arrays with circle air holes

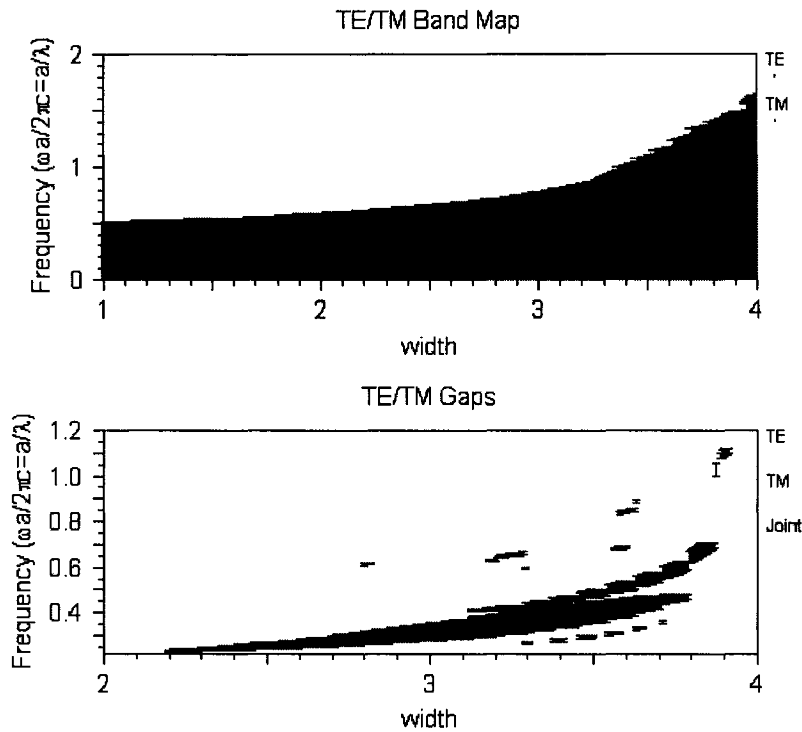

Figure 3.24 TE/TM Band Map and Gaps of square arrays with square air holes

Conclusion:

Figure3.22-3.24 denotes the functions of Band Map and Gaps with the sizes of air holes of three kinds of lattice arrays. They are direct and clear to show the relationship between the bandgap with the ratio of diameter (for hexagonal array with circle holes) or side (for square array with square holes) to air hole lattice constant. Thus, they are very important factors for the consideration of the optimizing design. For the hexagonal array with circle holes (showed in Figure 3.22), when the ratio of d/a is between 35%~50%, the PC structure can generate single narrow bandgap, and r/a is about 45%~50% as desired

value; for square array with circle air holes (showed in Figure 3.23), only the ratio of r/a reaches more than 67.5%, the PC structure exists bangaps, and two gaps appear at the same time; and for square array with square holes (showed in Figure 3.24), when the ratio of the width of air hole to lattice is between 55%~70%, the PC structure generates single bang gap, the ratio is about 55%~60%, can achieve desirable single narrow bandgap. Thus, the Figures 3.22~ 3.24 further show that the PC structures of hexagonal array with circle air holes and square array with square air holes can generate desirable single narrow bandgap, which are used to achieve narrow band Emitter/Detector. However, the narrow band gap is not the only consideration, we need to consider the application of the spectrum characteristics for the different purposes; for example, in our proposed design, we need our device provide conclusive identification and measurement of the target gas with little interference from other gases, so the extraction of light, FWHM of the radiation. For example, too narrow spectrum decreases the energy of emission.

3.3 Photonic Crystal Slabs (PCS)

3.3.1 Characteristics of emitted light from a 2-D PCS structure:

Two dimensions periodic structures are the common PBG application. In such structures, light is confined in the third dimension by traditional index guiding. Typical examples include waveguide slabs with a periodic set of holes/ rods of finite vertical extent. We refer to all such structures as Photonic Crystal Slabs (PCS) (showed in Figure 3.25) [24]. This PCS type consists of a structure with finite vertical height that is periodic

in two dimensions surrounded by a semi-infinite periodic cladding. Since the PCS structure does not contain defect regions for light generation, whole area of the photonic crystal can be used for both light generation and light extraction. PWM uses periodic boundary conditions in all directions. Thus in practice, the calculation of PCS performs a series of sets of holes/rods at equally space Y intervals. By increasing the size of the super cell, the simulation approximates a system where the structure is non-period in vertical direction.

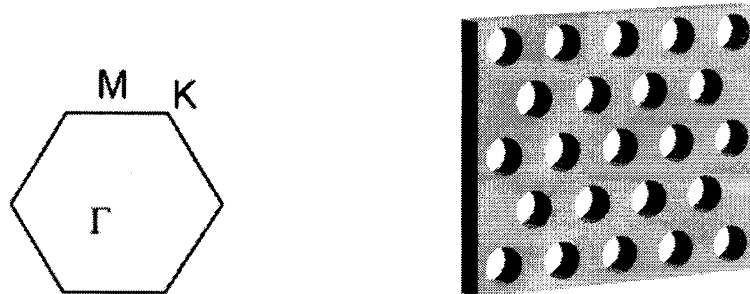

Figure 3.25 Photonic Crystal Slabs (PBS)

In the PCS structures, there are still leaky waveguide and radiation modes. These modes would eventually decay into the background material and are not guided. All these modes have an effective index lower than that of the cladding region. To remove these from the diagram, we employ a light line or light cone filter. This filter removes all of the radiation states from the band calculation.

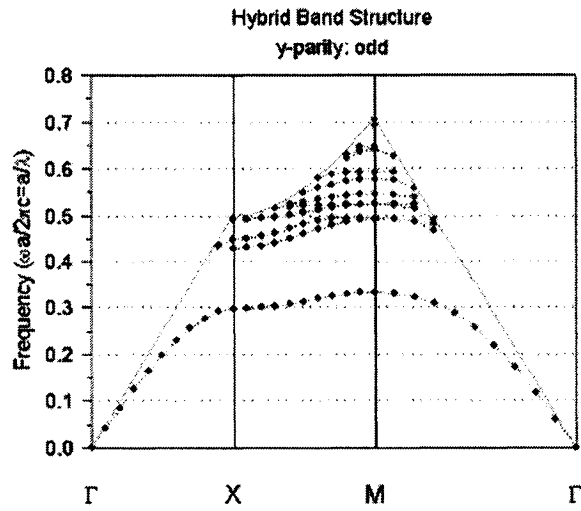

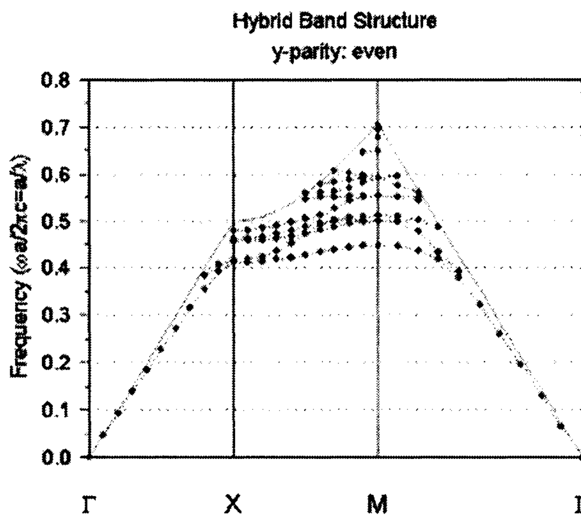

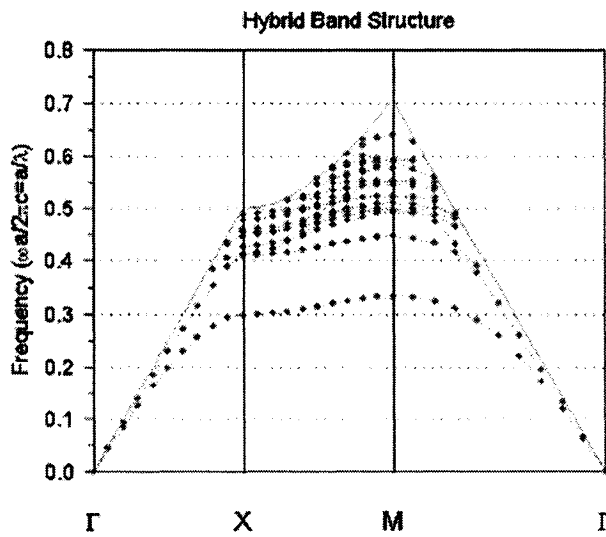

Figure 3.26 Even/odd of Photonic Crystal Slabs

Figure 3.26 shows the results of this calculation (hexagonal lattice). The use of the filter has added a "light line" to the band diagram and only bands below that line are shown. Emitted light whose frequency lies within the gap is therefore forced to couple to radiation states. The structure possesses one or more planes of reflection symmetry; the modes can be classified as either even or odd. These modes parallel the meaning of the TM and TE modes that are found in 1D and 2D structures. As a result, it is possible that a band gap exists between the even and odd bands of a PCS.

3.3.2 Enhancement of light Extraction from a (2-D) PCS [24] [35] [36]

It has recently been suggested that photonic crystal slab structures can enhance light extraction efficiency dramatically. Enhancement of light extraction efficiency from photonic crystal slabs relies on both geometrical properties and radiative properties of the structure. The light generated in the bandgap region can couple only to radiation mode since the guided modes are eliminated in the bandgap. In this case, the coupling of emitted light to free space modes results in significant enhancement of light extraction efficiency.

Fig. 3.27(a) shows a simple model consists of placing a point dipole source inside a uniform high-index dielectric slab. We choose a slab of thickness 0.5a, where a is an arbitrary length unit. The emitter radiation from the dipole source will either couple to guided modes of the dielectric slab or to radiation modes [35]. The existence of guided modes in the slab impedes the extraction of light.

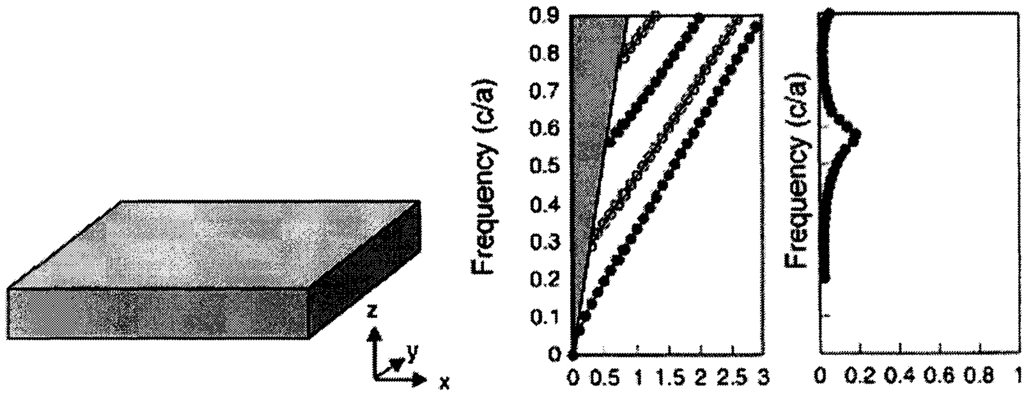

Figure 3.27 (a) uniform dielectric slab (b) Wave vector ($2\pi / a$) (c) Output efficiency[35]

In this case, the dispersion relation of the structure is shown in Fig.3.27 (b) for TE-like guided modes. The gray area corresponds to the continuum of extended (non-guided) modes. The solid circles correspond to TE guide modes with even symmetry with respect to the x-y symmetry plane, while the open circles correspond to TE guided modes with odd symmetry. Fig. 3.27 (c) is the output efficiency along the z direction. For the most part, the extraction efficiency is well below 10%.

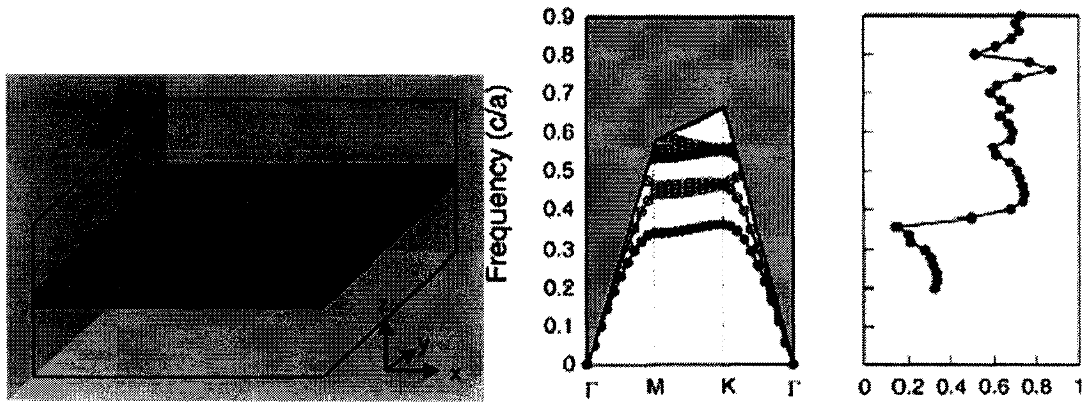

Figure 3.28 (a) Photonic crystal slab (b) Wave vector (c) Output efficiency [35]

Next, we introduce an index variation by patterning hexagonal lattice with air holes into the dielectric slab. The photonic band diagram for a corresponding slab with an

infinite array of holes is plotted in Figure 3.28. The gray region above the light line corresponds to the continuum of extended modes. Below the light line, that shows the bands for every guided mode in the structure. A gap can be seen in TE-like bands. The dipole is located at the center of the slab, and is aligned along the y direction. Only even TE-like modes will be able to couple to the emitted radiation. The output efficiency is shown in Figure 3.28(c). The efficiency alters around an average value of 70%. One important thing, only a finite number of holes are introduced into slab, some radiation is able to escape along the slab. The radiation intensity decays away from the source, up to the edge of the array, and couples to guides modes and remains trapped inside the slab. By increasing the number of holes, one should be able to achieve even higher extraction efficiencies.

3.3.3 PCS with bottom cladding

In the above example, we use a PCS structure, which is hexagonal array of air holes in a finite height dielectric slab. In our proposed device, the air holes will extend into the silicon substrate cladding. The upper cladding is air. In this case, the light line is defined by the minimum of the light lines for each cladding at each k-point. The light line for the lower cladding can be calculated via a 2D band calculation within the substrate. Because this structure type does not support parity, we can no longer divide the modes into even or odd types. Figure 3.29 shows the top view of the proposed structure: Hexagonal array of air holes PCS upon silicon substrate (lattice is 4 μm and radius of air holes is 1 μm). Figure 3.30 shows hybrid band structure of hexagonal arrays PCS with

bottom cladding. Figures 3.31 and 3.32 are the case of square lattice array of circle air holes PCS with bottom cladding.

Figure 3.29 Hexagonal array of air holes PCS with bottom cladding (a=4 μm; r=1 μm)

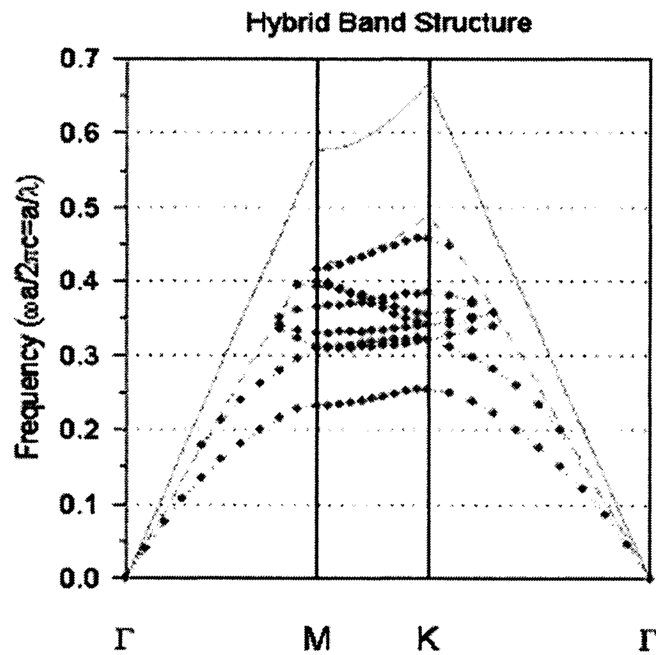

Figure 3.30 Hybrid band structure of hexagonal arrays PCS with bottom cladding

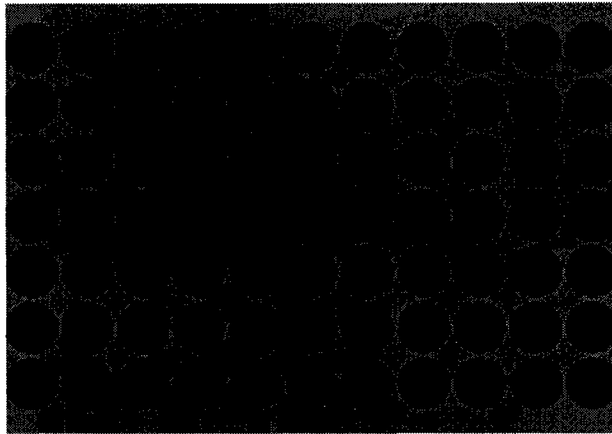

Figure 3.31 square array of air holes PCS upon silicon substrate

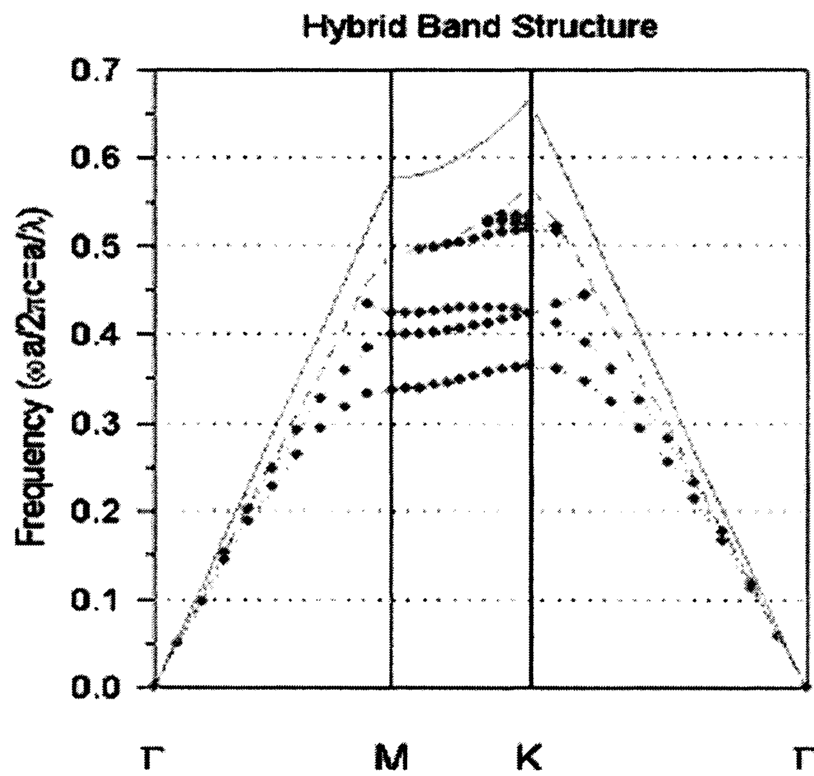

Figure 3.32 Hybrid Band structure of cubic array of air holes PCS with bottom cladding

3.3.4 The dependence of extraction efficiency on air-hole depth

Recently, some works [7] [23] show that the photonic crystal structures with air holes deeply etched have higher extraction efficiency than the shallowly etched structure. This large enhancement was benefited from the strong extraction ability of the photonic crystal slab and reduced surface recombination at low temperature. The efficiency of light extraction from a photonic crystal slab can be calculated using the three- dimensional (3D) finite difference time domain (FDTD) method (that will be discussed in Appendix) by altering the finite depth of air-hole patterns. The other group has investigated the effect of holes depth on the controlled emission from these surfaces [7]. Figure 3.33 shows that the inband reflection is decreased along with an increase in inband absorption when the depth is increased. According the Kirchhoff's law, a strong absorber will correspondingly exhibit strong thermal emission properties. Therefore, the deeper air holes PC structures achieve stronger emission. In addition, the extraction behaviors of a hexagonal lattice and a square lattice are compared, and it is shown that their distinctive extraction characteristics well reflect the features of each band structure.

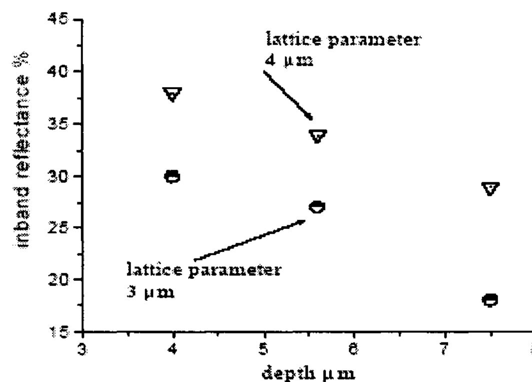

Figure 3.33 inband reflectance versus holes' depth [7]

3.4 Optimization of the electrical properties of the proposed device

Fundamentally the proposed model is concerned with the thermal response of the proposed device using temperature dependent thermal conductivity, specific heat, and electrical resistance to calculate conduction, convection, and radiation losses for negative temperature coefficient of resistance material [21]. As shown elsewhere [21] [37], the emission spectrum could be approximated by a series of two to four Gaussian curves where the central wavelength and full-width at half- maximum (FWHM) did not change with temperature. The peak height of these Gaussian curves was equal to that of a blackbody at the given temperature and wavelength. Relative heights of each Gaussian curve would be altered with temperature. Some people design a mode with ten micron thick (PC requirements) and $3mm^2$ area for optical alignment achievable in production [21]. They calculated the temperature profile with power in fixed geometry by the finite element approach (show as Figure 3.34).

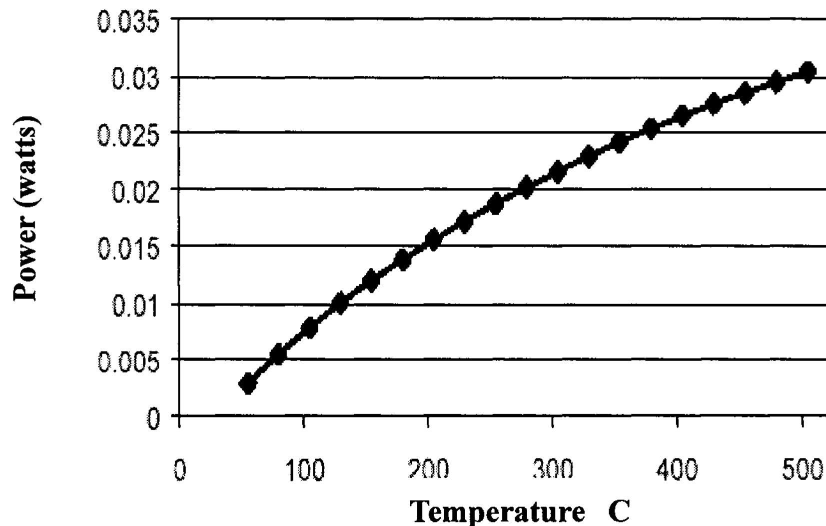

Figure 3.34 The temperature profile versus power [21]

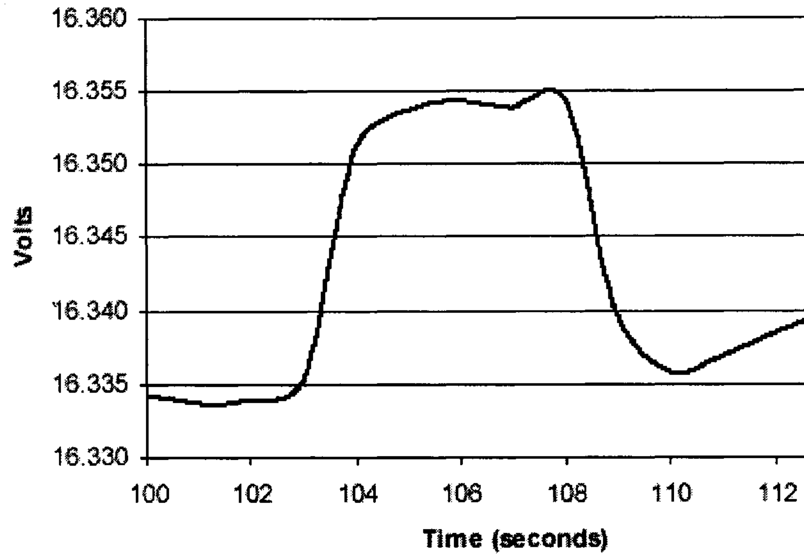

Figure 3.35 The increase of power supply to maintain the fixed temperature as shutter in light path [21]

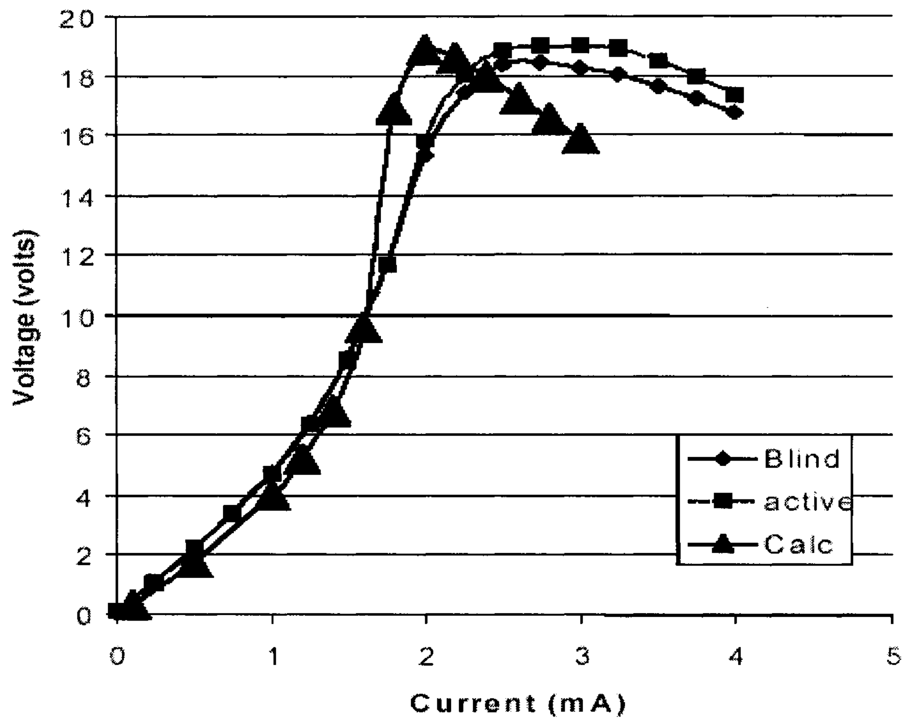

Figure 3.36 the current-voltage curve [21]

Figure 3.35 shows the measurement parameters of the sensor. In this example,

power was supplied to the silicon only (not metal). A shutter between the emitter/detector and mirror was employed. The digital logic power was used to maintain the sensor at a fixed temperature (resistance) to compensate for the negative temperature coefficient of resistance of silicon. For this calculation, the optical path was blocked by a shutter suddenly placed into and then removed from the test cell. With reflected light blocked, the sensor would cool and the power supply, commanded to maintain a fixed temperature, need increased voltage to compensate. Figure 3.36 shows a complete current- voltage curve. Thermal conduction at high power varies as true temperature profile changes with convection.

CHAPTER IV

DESIGN AND FABRICATION

In this chapter, the design and fabrication of the device according to the previous conclusions about the structure, materials and the optimum values of geometry parameters is discussed.

4.1 The structures, materials and geometry parameters

4.1.1 The structures

It is known that photonic crystal (PC) structures can generate narrow band infrared radiation, and "hole" type PC structures are suitable for the generation and propagation of defined wavelength light in the substrate. Generally, this narrow emission band derives from phonon interactions in the silicon-air PC, and combines with surface plasmon resonances in the perforated metal surface. These resonances induce photon emissions at discrete wave vectors defined by the lattice parameter of the PC. We created the structure in micro-bridge geometry to enable power-efficient heating of the device and to enhance its sensitivity to gas concentration since the drop in temperature is proportional to the concentration of the target gas, and it is more sensitive to changes in resistance or voltage across the bridge.

4.1.2 The materials

Optimally, we know that single silicon is desirable material for the photonic crystal (PC) structure to achieve the stable narrow band emission; gold has excellent

characteristics in electrical, mechanical and chemical for surface plasmon. Moreover, the most standard MEMS technology process uses these materials to fabricate devices.

4.1.3. Geometry parameters

According to the discussion of previous chapter regarding the optimization geometry parameters, the optimum geometry parameters are summarized in Table 4-1.

Table 4-1

Lattice arrays	lattice	d/a (w/a)	holes depth	device sizes
Hexagonal (with circle holes)	$\lambda \approx \sqrt{3}a/2$	45~50%	4~7 μm	$3\,mm^2$
Square (with square holes)	$\lambda \approx a$	55~60%	4~7 μm	$3\,mm^2$

a. Lattice constant

The reflection spectrum dominated by a single sharp feature corresponding to the lowest plasmon order. In the section of surface plamons dispersion relation, we knew that there is three factors affect the resonances: the lattice periodicity, the dielectric properties of the material below the metal, and the depth of the air holes in the PC. For square arrays, the central wavelength is approximately equal to the lattice constant ($\lambda \approx a$); and for hexagonal arrays, there is the relationship between the fundamental SP mode wavelength value and lattice constant ($\lambda \approx \sqrt{3}a/2$). From the spectra, there are comparable simulation results between the hexagonal arrays with circles and square arrays with

square holes. Both of them can achieve narrow band infrared light, which the wavelength of resonance defined by the lattice spacing of the crystals, with little interference from other gases. The little difference is the hexagonal arrays exhibit an exceedingly narrow full-width half- maximum (FWHM), where the incident wave is absorbed by the sharp SP resonance on the gold substrate. The narrow FWHM corresponds to $\Delta\lambda / \lambda_0 = 0.05$, and for square trench with the same width and depth as the circular feature has a slight increase of line width to $\Delta\lambda / \lambda_0 = 0.06$ [3].

b. The ratio of d/a (w/a)

In optimum geometry, we knew that there are optimum values of the rate of 45% ~50% holes diameter to lattice (d/a) for hexagonal array PC with circle holes and the rate of 55%~60% holes width to lattice (w/a) for square array PC with square holes can achieve desirable single narrow bandgap that result narrow band emission. The square array PC with circle structure that the rate (d/a) is more than 67.5% can generate bandgaps, and two gaps at the same time.

c. The depth of holes

In the light extraction efficiency, we knew that the deep air hole structure have higher absorption characteristic that result higher emission. Although the structure of air holes entirely drilled through the PCS can achieve the highest extraction. The extraction efficiency is defined as the fraction of emitted flux through the top and bottom surfaces of slab to the total emitted flux, only top emitted light will be used in our proposed device; furthermore, the device services as both emitter and detector, the reflected light from the

mirror will be absorbed in the sidewall and bottom of the air holes. Therefore, we need to choose thicker silicon substrate (more than ten micron), and etched the depth of air hole about 4 to 7 microns.

d. The type of holes

An important property of Photonic Crystal structures is that the air holes must be vertical, which make incoming light line at small angle of incidence to the surface. This needs to use dry etching processing, such as deep reactive ion etching (DRIE).

4.2 The choice of the fabrication process

In order to fabricate this kind of structure, we need to choose a suitable technology process. We tried to find a standard fabrication process to do some fundamental research work. Firstly, CMOS processing is not suitable because the device layers are too thin. Next, we considered PolyMUMPs processing, one of popular MEMS technology; we found it impossible because the thickness of poly 2 is 1.5 μm and poly 1 is 2 μm. If we use poly2 as PCS and poly1 as bottom cladding, the light extraction efficiency should be much lower; moreover, metal layer was patterned (lift-off) onto the poly2 that asked the poly2 at least enclose the metal layer 3 μm; however, the feature / space sizes of our proposed device is only about 2 μm; furthermore, we hope our device construct into micro-bridge in order to improve its sensitivity. But this process needs to use additional air holes in the structure to release the device, and the maximum distance between etching holes is 30 μm. That means we need to etch many undesirable holes to

release the micro-bridge structure. The undesirable holes will be defect points of photonic crystal that alter the light propagation characteristic.

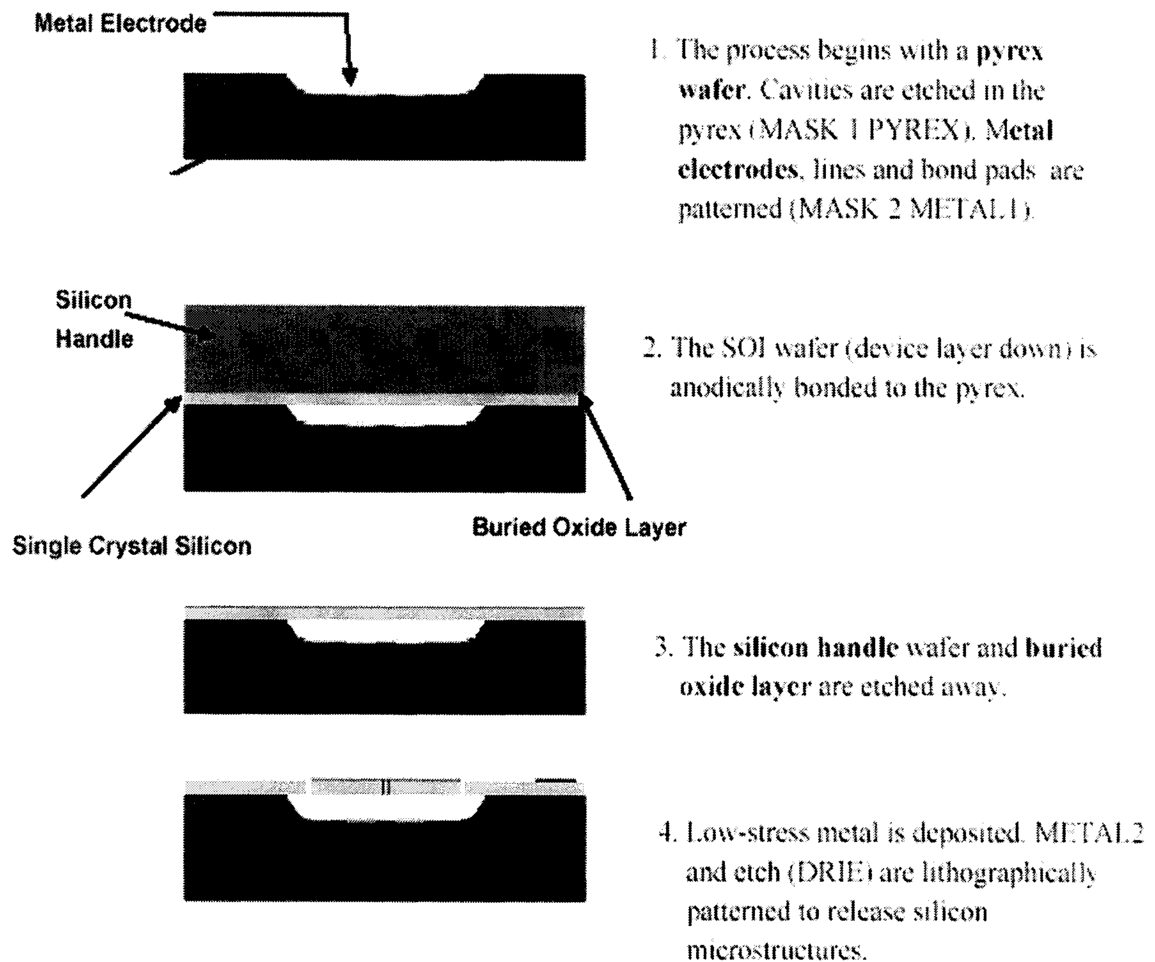

Figure 4.1 Standard MicraGEM fabrication process

This year (2004), CMC and Micralyne Inc. provided new micro-electro-mechanical systems (MEMS) prototyping process that allows designers to vary the thickness of structural layers (two options), thus adding more functionality to their designs. This silicon-on-insulator (SOI) based micromachining process, called

MicraGEM (Micralyne GEneralized MEMS), and allows users to develop fully suspended MEMS devices with metal electrodes. The standard MicraGEM processing is described in Figure 4.1.

We applied for option A, which the substrate is10.3 μm thick single silicon crystal. Metal 2 (750 A^{o} thick gold) was used as surface plasmon, electrodes and bonding pads. Another important parameter of the design rules is the minimum feature and space sizes are 2 μm. From the discussion above, we can see that this fabrication processing is not perfect but in the range of tolerance. We have designed the proposed device in different structures and parameters without breaking the design rules.

4.3 Fabrication technology and design

4.3.1 Fabrication processing

We used this fabrication process (option A) to design the proposed device (Figure 4.2 is the side view of the device; Figure 4.3 is the top view of it, and Figure 4.4 shows 3 Dimension (3D) models of two kinds of typical lattice arrays):

1. The first step is to open a cavity within Pyrex wafer by using isotropic wet chemical etching process in order to making the device fully suspended micro-bridge structure.
2. Next, the SOI wafer (device layer down) is bonded to the Pyrex by the assistance of the silicon handle.
3. The handle and buried oxide portions of the wafer are etched away in a wet

process, leaving the single crystal silicon membrane above the cavities/gaps.

4. Chrome/gold (METAL2) layer is deposited on the silicon surface.
5. Part of METAL2 is etched to expose the silicon using a wet etching; this process services as constructing the profiles of the device, electrode, and bonding pads.
6. The last lithography of etch steps is with MASK4 (DRIE). In design rules, the minimum figure and space sizes of metal2 are $2\,\mu m$. We kept the metal2 layer upper PC during the metal wet etching, and use DRIE to etch the holes pass through metal into silicon layer. In this way, we needn't consider the alignment of the holes in both layers.
7. The electron-beam lithography was used to texture the surface of the emitter/ detector for a much more precise and narrow wavelength selectivity. The ion-beam etching exhibits increased optical absorption over a defined wavelength band, and emits preferentially over the same wavelength band when heated.

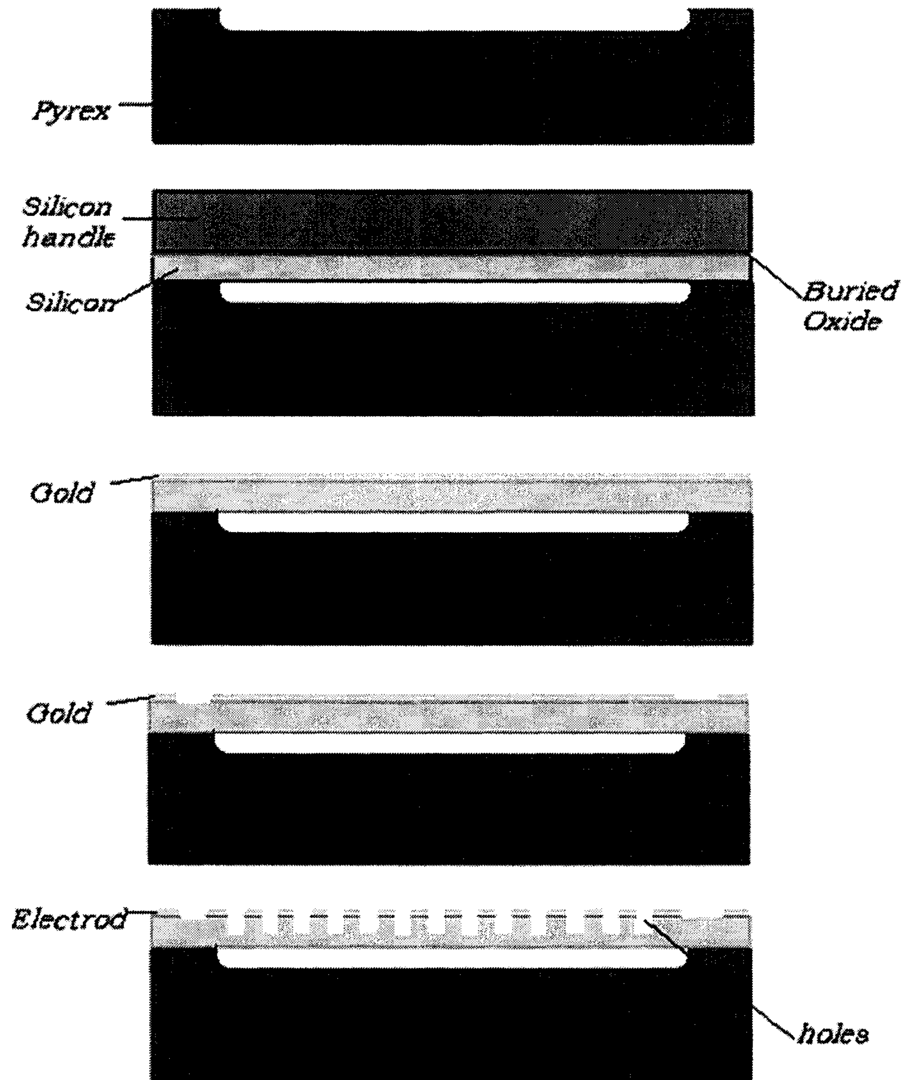

Figure 4.2 Side view of our proposed device

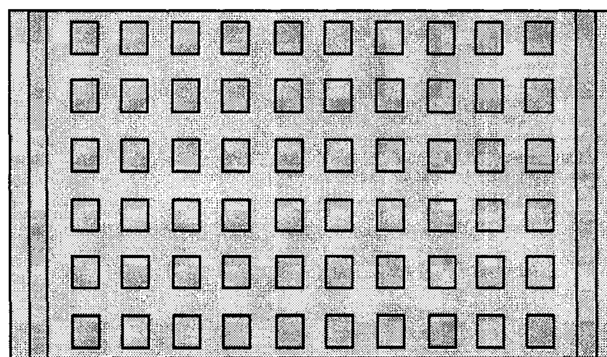

Figure 4.3 Top view of our proposed device

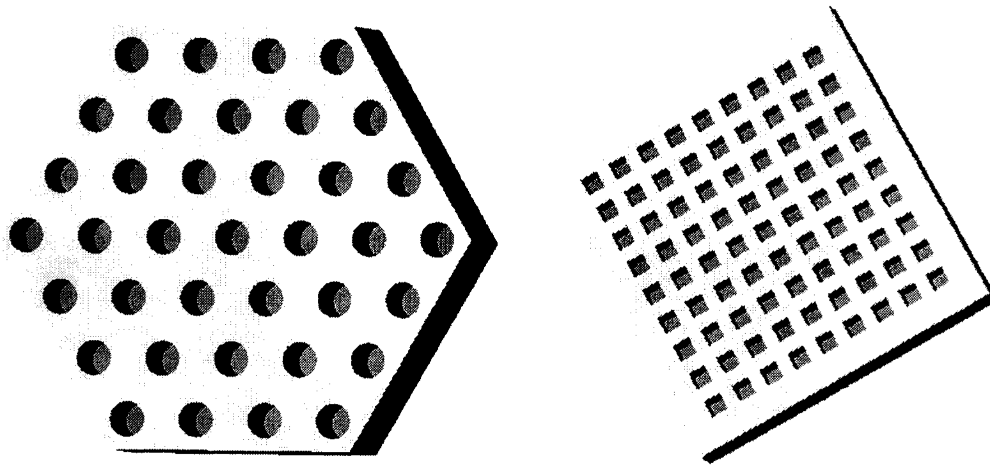

Figure 4.4 The 3 Dimensions (3D) models of two kinds of typical lattice arrays

4.3.2 The advantages of MicraGEM processing for proposed devices

1. Single silicon will be used in the device layer. It appears not only stable narrow band emission, but also it has higher resistant coefficient that will improve the sensitivity of the device's temperature, combining the micro-bridge structure
2. The thicker silicon layer of the device corresponds to Option A (10.3 μm) can be possible for us to etch deeper holes to improve the emission and absorption of the device, reduce surface recombination.
3. This silicon on isolator (SOI) process enables to develop fully suspended MEMS devices with metal electrodes (rather than silicon). This structure is more suitable to design bigger area micro-bridge structure, avoid putting the undesirable holes to release the device.
4. An important design about the mask of metal2 layer, we designed separated

electrodes, wires and bonding pads, and did not design air holes in metal2 layer. Also, we put full area metal upper the PC position. We designed the air holes only in silicon layer. In this way, wet etching (isotropic) of gold keeps the electrodes, wires, and bounding pads, and full area metal upper the PC position. DRIE (anisotropic) pass through the metal layer into the silicon layer in defined depth to achieve PC and surface plasmon structures.

5. A simple lithographic mask change allows changing the spectral tuning of the micro-bridge in production. In concrete, only change the lattice of the MASK4 (DRIE), we can produce different gas sensors, such as CO, CO_2, and so on.

4.3.3 Design of the proposed devices

For most real application, performing a single band structure calculation is insufficient. In order to create a workable structure, the designer needs to identify important parameters and optimize their values to achieve the desired results. A related problem is to evaluate the acceptable tolerances in design parameters. According to the optimum geometry structures and parameters combining with fabrication design rules, 16 devices were designed, which the parameters are displayed in table 4.1 and layout in Figure 4.5, in three kinds of lattice array: hexagonal lattice array with circle holes, square lattice array with square holes and circle holes.

Table 4-2 Device diameters:

Arrays	Hole types	Holes Diameter (μm)	Space Sizes (μm)
Square	Square	2.5	2
Square	Square	3	2
Square	Square	3.5	2.5
Square	Square	2	2
Square	Square	2.5	2.5
Square	Square	3	3
Square	Square	3	2
Square	Square	2	2
Square	Circle	2	2
Square	Circle	3	3
Square	Circle	2.5	2
Square	Circle	3	2
Square	Circle	2.5	2.5
Hexagonal	Circle	2	2
Hexagonal	Circle	2.5	2.5
Hexagonal	Circle	3	3

In these devices, it is tried to change the sizes of holes and spaces in the ranges of optimum values: $d/a=1$ for hexagonal lattice array with circle holes, $w/a \approx 55\%\sim60\%$ for square array with square holes.

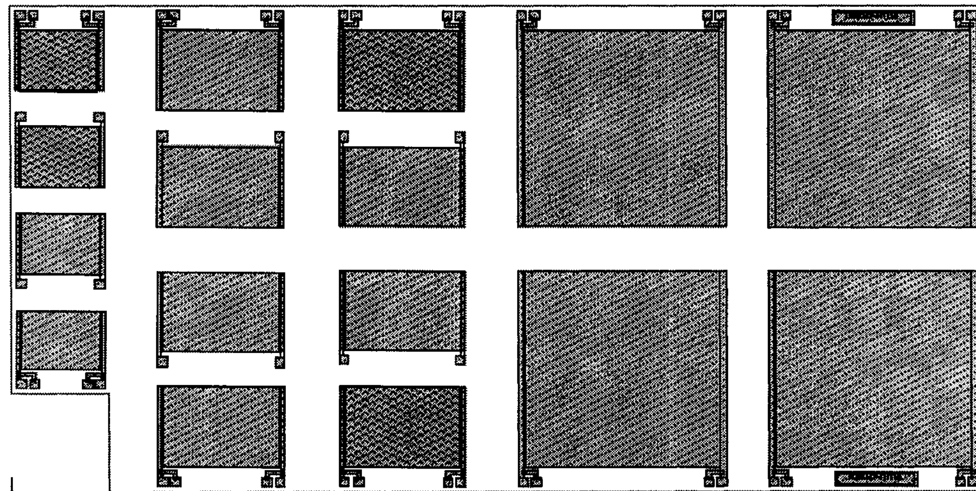

Figure 4.5 the layout of the devices

Figure 4.6 and 4.7 shows the TE PBG simulation results of two typical square arrays with square holes. It is tried to find the relationship between wavelengths with lattices, and the bandwidth of emission light with d/a (or: w/a) in different lattice array.

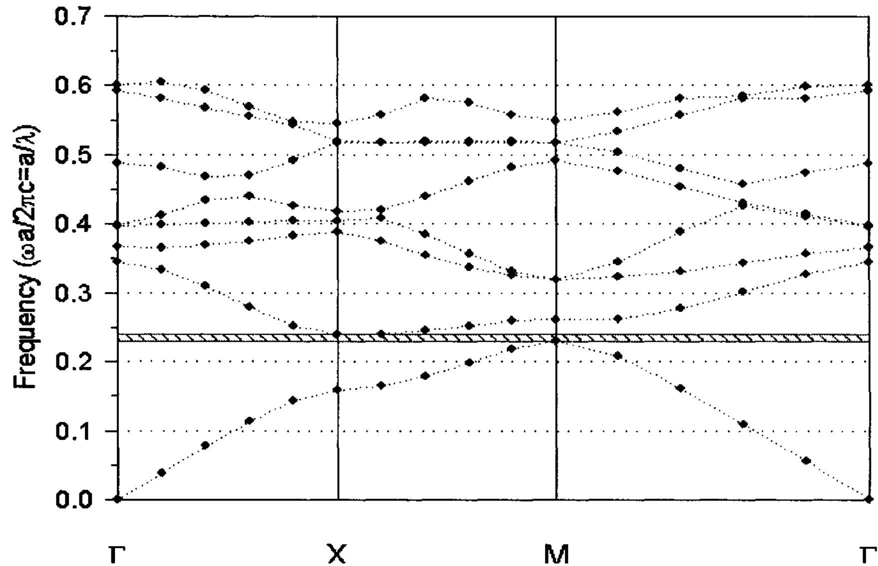

Figure 4.6 TE PCB of square array with square holes

(a=4.5 μm; w=2.5 μm; n=3.42)

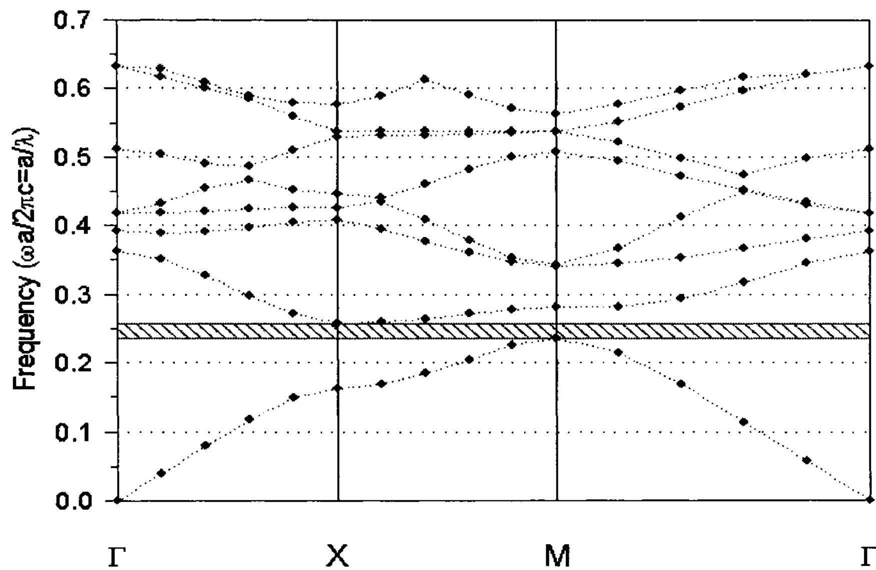

Figure 4.7 TE PCB of square array with square holes

(a=5 μm; width=3 μm; n=3.42)

4.4 The simulation results of the proposed devices

The simulation of the proposed device is used to calculate the electromagnetic field as a function of time and space for a given index structure in response to a given excitation, and display the field dispersion at selected time intervals. It is frequently useful to record this field information as a function of time or frequency for post processing and analysis purposes. The simulations used the famous finite difference time domain (FDTD) calculation method, and perfectly matched layer (PML) and periodic boundary condition (PBC) were used as boundary conditions. Appendix II will explain these concepts in more details.

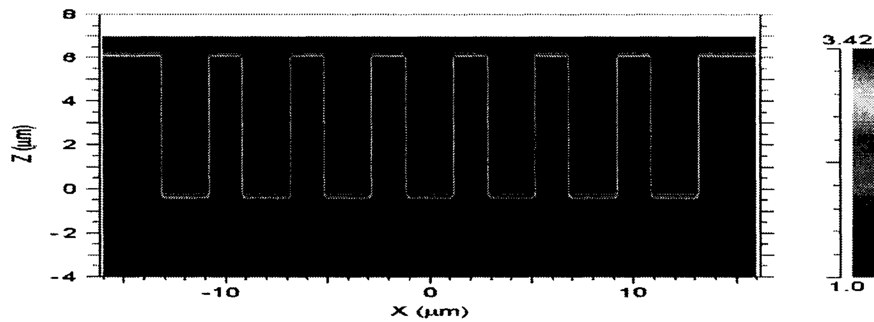

Figure 4.8 Index distribution of the square lattice array with square holes (Side view)

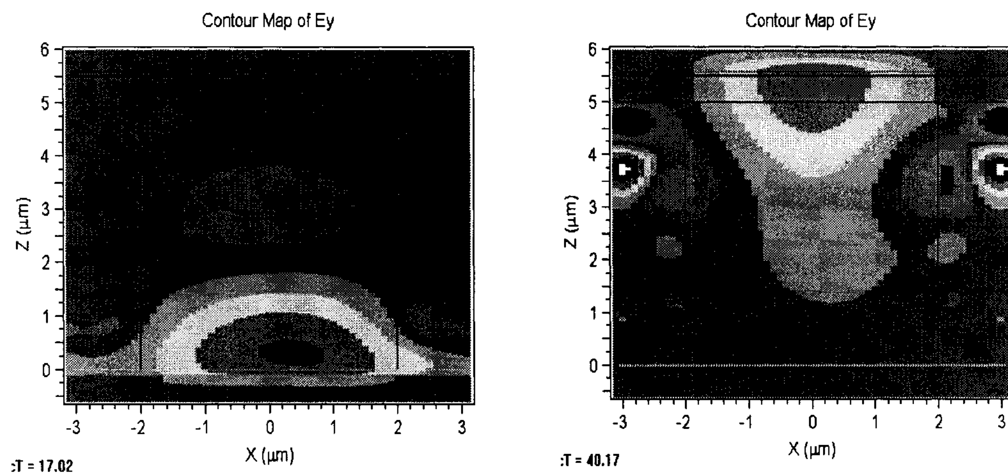

Figure 4.9 Simulation process of single cell

The side view of index distribution of the square lattice array with square holes is displayed in Figure 4.8. Figure 4.9 shows the simulation process of single cell in time monitor. The incoming light (electromagnetic waves) that is launched lies within a range of photonic bandgap frequency cannot propagate along the photonic crystal plane directions; however, they can propagate in vertical direction of the crystal. When they reach the surface, parts of them pass through the holes of perforated metal films, and others incident metal film acts as plasmons propagate in the surface.

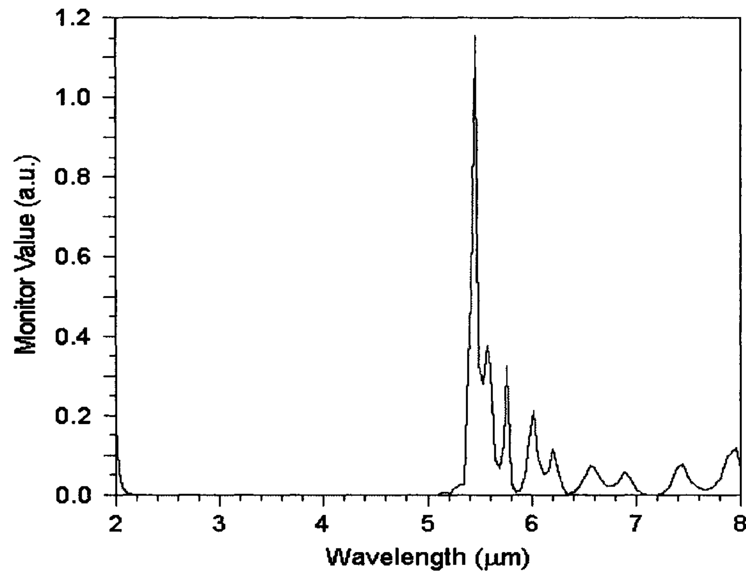

Figure 4.10 The simulation result of the proposed device

Figure 4.10 is the output spectrum of the simulation that shows the resonance wavelength of the proposed device. We can see that the structure of photonic crystal combine with surface plasmon technology can generate narrow band infrared light. The relationship between the resonance wavelengths with lattice for square lattice array with square air holes illustrated as in Fig. 4.11.

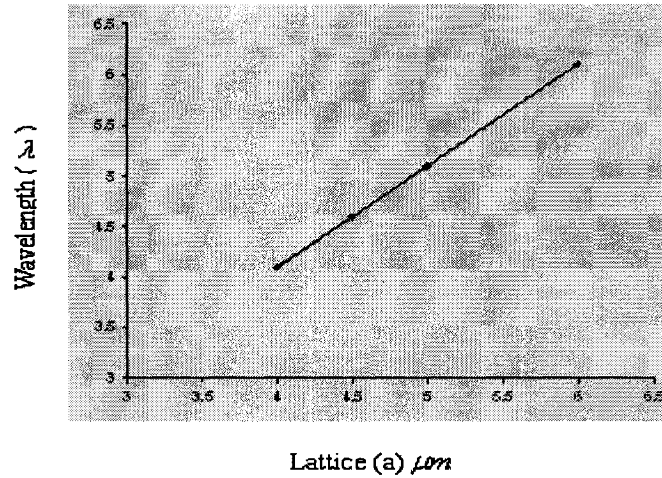

Figure 4.11 the relationship of resonance wavelength and lattice for square lattice array with square air holes (w/a ≈ 55%~60%)

We observed a linear dependence between wavelength of resonance and the lattice of periodic array, and wavelength and lattice constant is approximately equal. Similarly, there is also an approximate linear relationship between the resonance wavelength and the lattice for hexagonal array with the circle holes, as illustrate in Figure 4.12, and domain wavelength and lattice have an approximate relationship of $\lambda \approx \sqrt{3}a/2$.

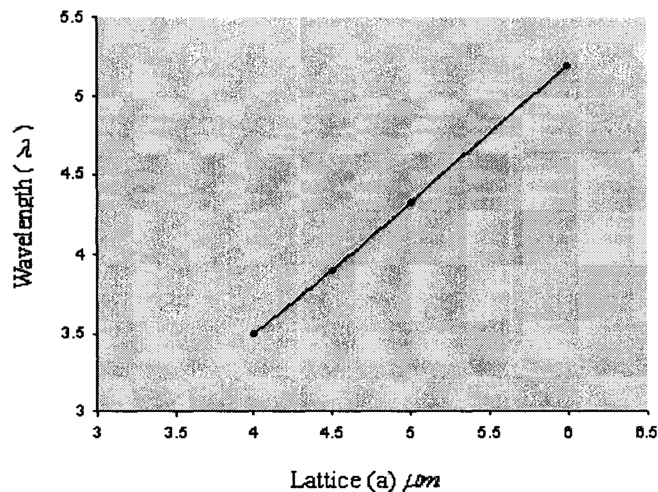

Figure 4.12 the relationship of resonance wavelength and lattice for hexagonal lattice array with circle air holes (d/a=1)

4.5 Fabrication results and analysis:

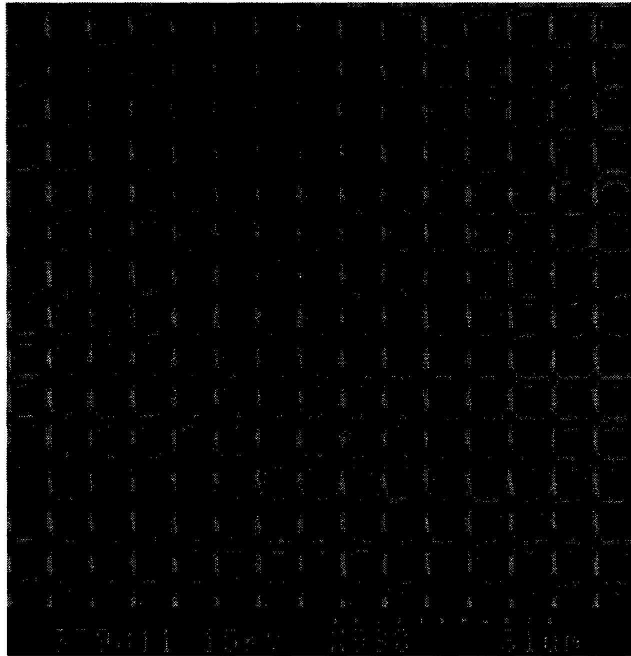

Figure 4.13 (a)

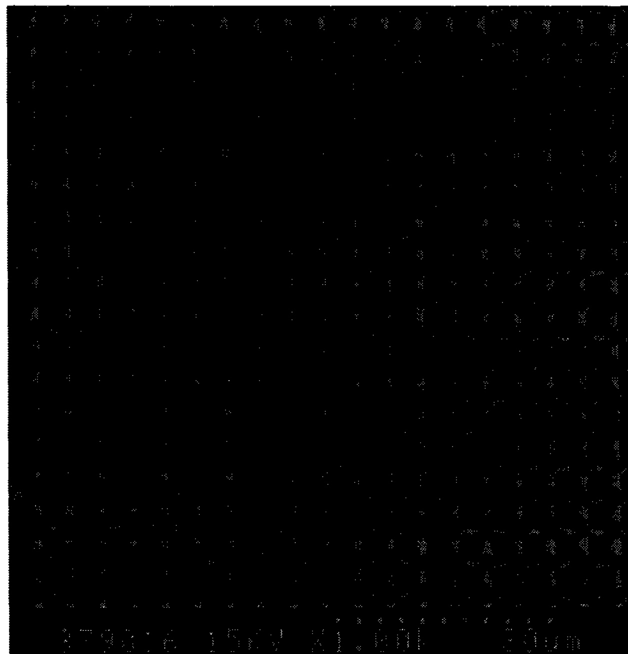

Figure 4.13 (b)

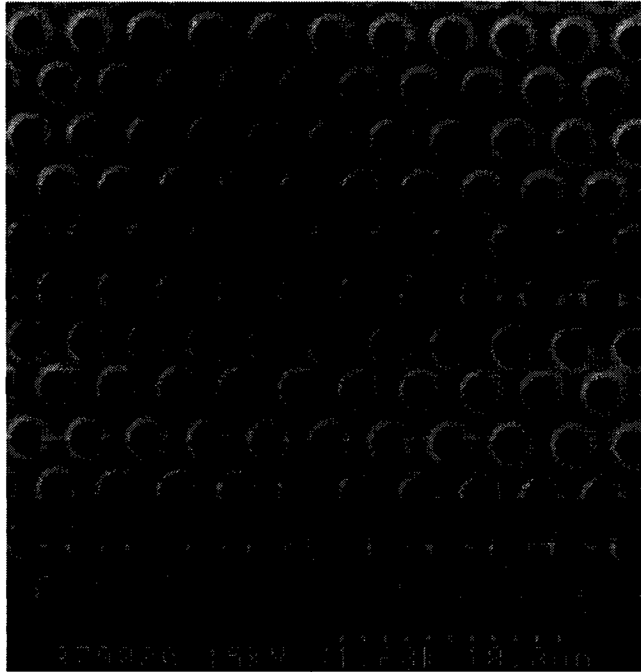

Figure 4.13 (c)

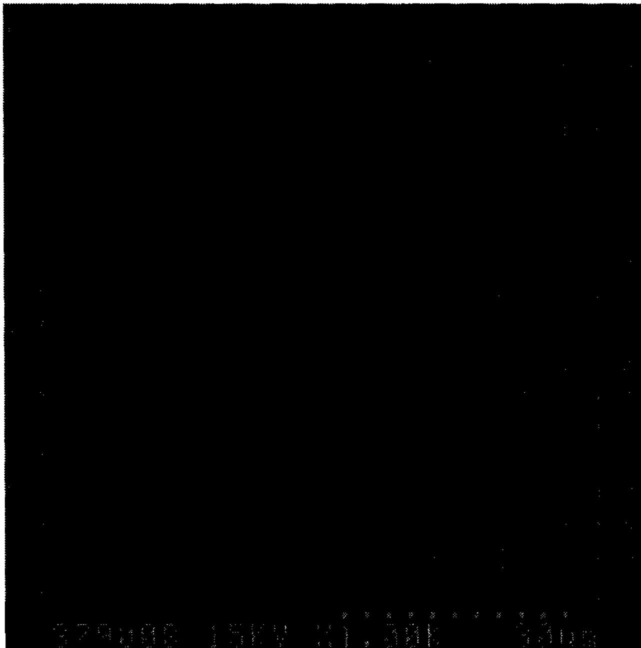

Figure 4.13 (d)

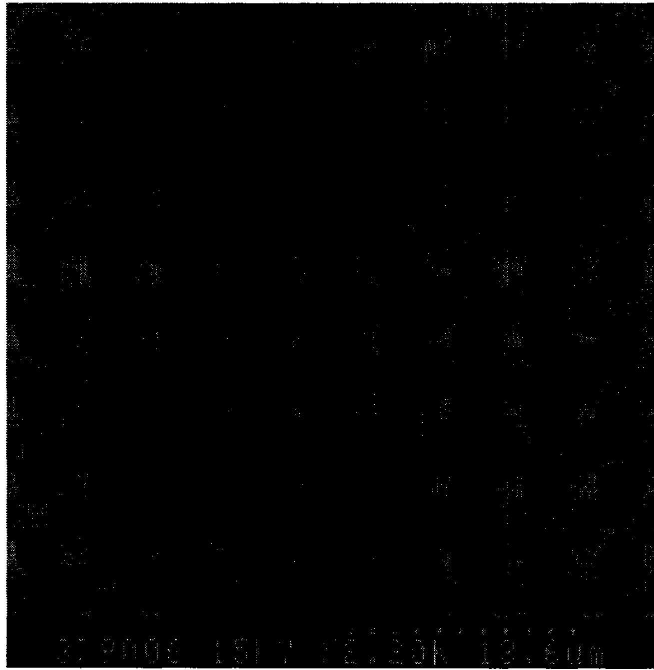

Figure 4.13 (e)

Figure 4.13 (f)

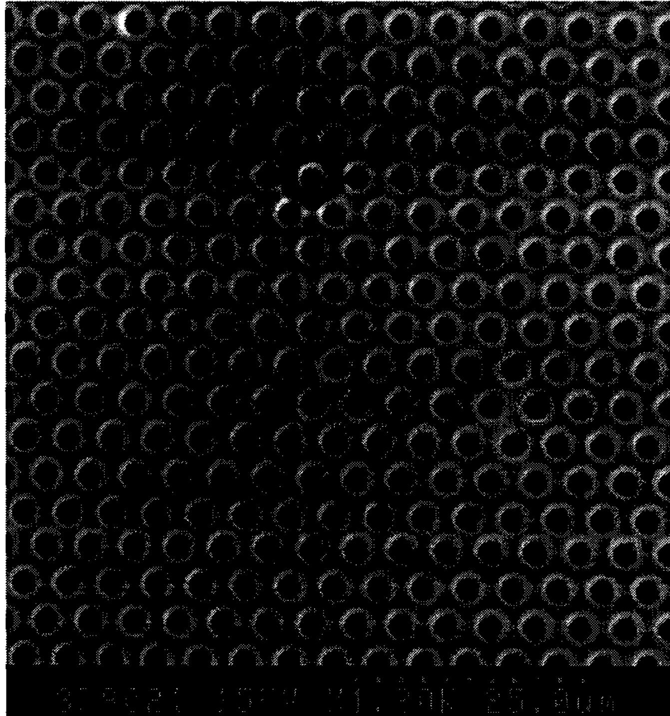

Figure 4.13 (g)

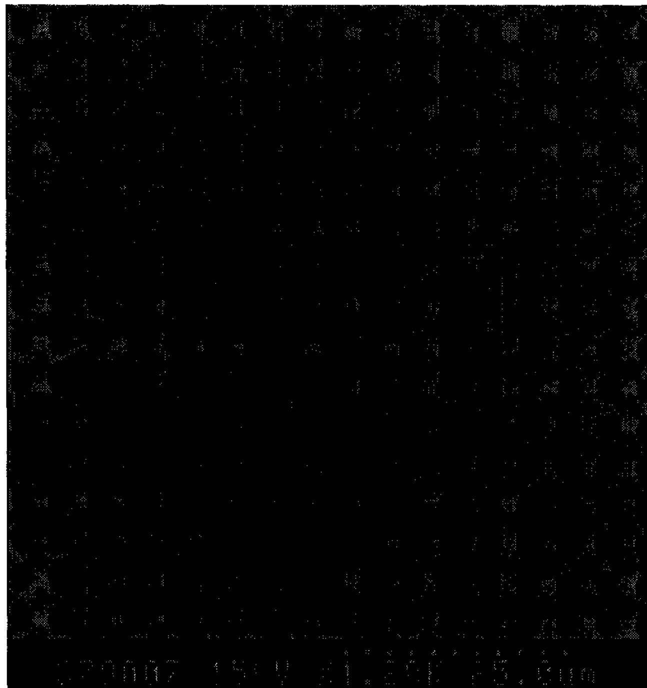

Figure 4.13 (h)

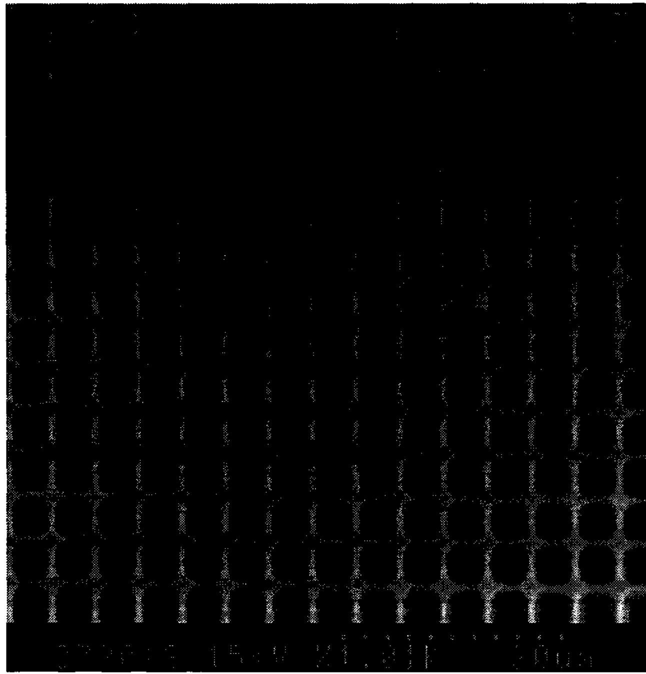

Figure 4.13 (i)

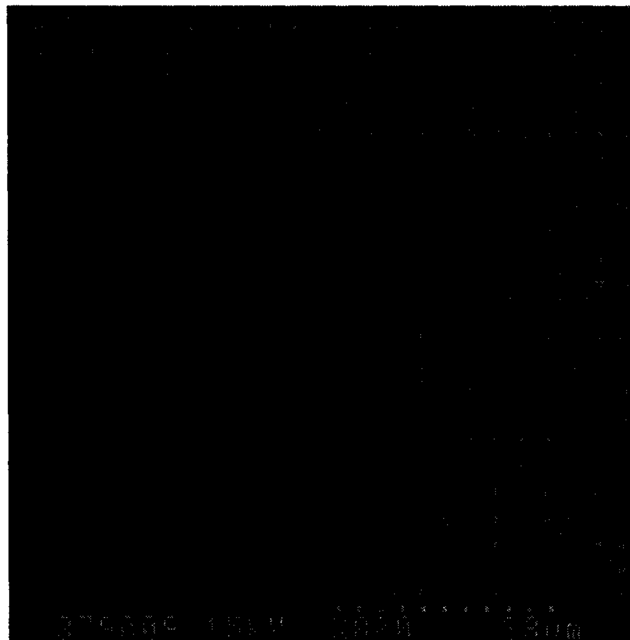

Figure 4.13 (j)

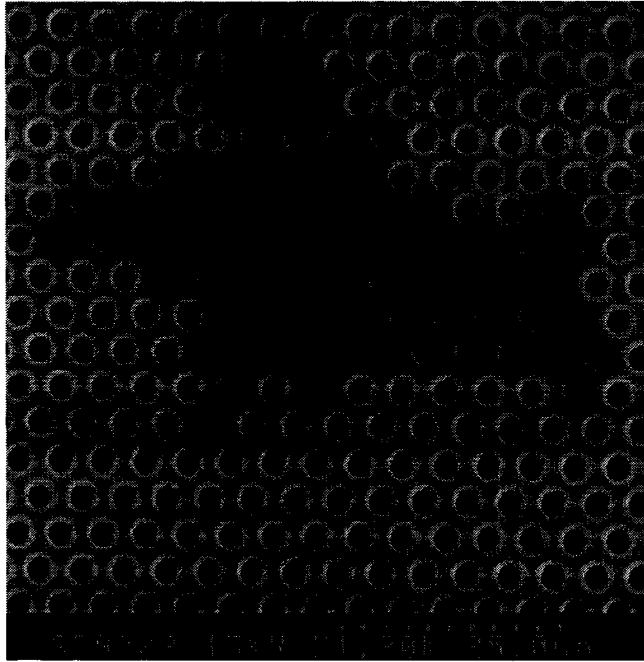

Figure 4.13 (k)

Figure 4.13 (l)

Analysis:

Figure 4.13 (a-k), show Scanning Electron Microscope (SEM) pictures of parts of the devices that fabricated by Silicon-On-Isolator (SOI) standard technology process, which is the test run from the CMC and Micralyne Inc. Unfortunately, the devices could not be successfully fabricated although our design did not break any design rules. The main reason was that this process provided error design rules in minimum size of self-alignment etching. According to the optimization of geometry parameters, we need design the hole around minimum size of the design rules in tolerance. Figures 4.13 (a-f) shows those parts of the devices that were well developed during the fabrication. We can see three kinds of lattice arrays: hexagonal array with circle holes, square arrays with square and circle holes, with different feature and space sizes. Figures 4.13 (g-k) show that the fabrication failed. Figures 4.13 (g, h) display the metal film over etched. Figure 4.13(i) shows the defect points due to not completely etched metal layer. Figures 4.13(j, k) show bigger areas of the structures that are not completely etched. Although DRIE pass through the metal layer, the silicon layer is almost not etched. Finally, Figure 4.14 (l) is shown the whole device. We can see that most parts of the device were not etched completely.

We could not test any of these devices because all of them were damaged during the fabrication. The most part of the air holes were not etched completely. We were unable to find an area for the germanium sphere element of ATR to touch the samples. To the benefit of the readers the measurement methods are introduced in Appendix I.

CHAPTER V

CONCLUSIONS, SUGGESTIONS, AND FUTURE WORK

This thesis discussed MEMS spectroscope gas sensor based on photonic crystals and surface plasmon technologies by modeling combined thermal, electrical, optical and mechanical response. In the theory analysis, we have shown that gas sensors based on each gas have a range of particular wavelengths absorption characteristics. The innovation of MEMS infrared gas sensors integrate the optical filter, detector, and IR source into a single device, which generate high extraction narrow band infrared light concentrated on the target gas, and serves as Emitter/Detector. The TE and TM PBG in three lattice arrays, and optimization of the structure, material, geometry, and electrical properties are discussed.

We also designed and fabricated the different structure proposed gas sensors in tolerance design rules by utilizing Silicon on Isolator (SOI) technology of MEMS, which provided by Canadian Microelectronic Corporation (CMC) and Micralyne Incorporation. Unfortunately, the devices could not be successfully fabricated although our design did not break any design rule. However, our design help Micralyne to identify the minimum size of the etch holes for silicon which was unknown before. Moreover, it has helped CMC to evaluate Micralyne's fabrication ability and redefine the designed rules for etch holes. So this was not a design error rather, it proved to be a process error. It also helps for Micralyne to improve MicraGEM process. CMC and Micralyne are planning a second test run using the improved MicraGEM process for further evaluation. The new test run

based on the feedback (conference call) received from all the designers of previous run. It updates the following changes in MicraGEM:

♦ It added a second option for cavity etch. Now the designer can make cavity gap in three options (2 μm or 10 μm or together 12 μm).

♦ It added a M1 to M2 connection through the silicon. This will enable to develop microchannels with embedded electrodes accessed externally. This was also demanded for RF application.

♦ It only offers one thickness of silicon layer (10 μm) instead of both the 2 μm and 10 μm offered previously. Generally designer required thicker layers.

♦ There will be two different die sizes. Not yet decided the sizes but shall be smaller equal to or smaller than 5mmby 10mm.

♦ Micralyne will perform Resistivity measurements of Metal 1, Metal 2.

♦ Micralyne will perform Stress measurements (with temperature cycling) of Metal 1, Metal 2.

♦ Micralyne will perform Cr/Au feature size tolerance testing. (Wires vs. holes, undercut, change of metal to Ti/W/Au is under discussion).

♦ Micralyne will perform testing of M1 to M2 connections.

♦ Micralyne will perform DRIE testing/characterization to improve the quality of side walls.

The Updated user manual and technology files will be available by end of this year (2004). This SOI MEMS processing has a potential for mass production application.

We hope Micralyne and CMC improve fabrication technology process to make it perfectly.

5.1 Conclusion:

1. The "holes" PC structures are suitable for proposed gas sensors by generating and propagating of the infrared light in bulk silicon.
2. Micro-bridge structures of proposed device improve power-efficient heating of the device and enhance its sensitivity to gas concentration.
3. The gold material has good characteristics for surface plasmon in electrical, chemistry, and mechanical; and silicon material is better choice for generating stable narrow bandwidth of light comparing with SiO_2 and SiN.
4. The dielectric layer in contact with the metal along with the lattice constant of the array will influence the position of the resonance.
5. For square arrays, the central wavelength is approximately equal to the lattice constant ($\lambda \approx a$); and for hexagonal arrays, the relationship between the fundamental SP mode wavelength value and lattice constant is $\lambda \approx \sqrt{3}a/2$.
6. The resonance wavelengths are liner dependence with the lattice in hexagonal and square patterns in defined materials.
7. The optimum values of the rate of 45% ~50% holes diameter to lattice constant (d/a) for hexagonal pattern of circle holes and the rate of

55%~60% holes width to lattice constant (w/a) for square lattice of square holes can achieve desirable single narrow bandgap that result narrow band emission. The hexagonal pattern can achieve smaller FWHM than square Pattern.

8. In order to improve the light extraction, we need to choose thicker silicon substrate (more than ten micron), and etched the depth of air hole about 4 to 7 μm. MicraGEM processing (option A) provide thicker single silicon layer (10.3 micron)

9. The sample diameter should be more than 2mm for the sphere germanium element of ATR to touch the sample. The sizes of device should be bigger than 3 mm^2 for reflected light alignment.

10. The applied voltage is less than 16V, and the power is about thirties mw.

11. SOI MEMS fabrication process can achieve full-suspended micro-bridge structures for proposed device, which improves the sensitivity of the device to the temperature.

12. A simple lithographic mask change allows us to change the spectral tuning of the micro-bridge in production.

13. DRIE processing allows the ion beam pass through the metal layer into the silicon layer in certain depth. This ensures the same vertical profile of air holes in both layers.

5.2 Suggestions:

1. **Using hexagonal pattern of the circle holes**

   Both PC structures of the hexagonal pattern with circle holes and square pattern with square holes can achieve single narrow PCB that result narrow band emission. The optimum value is that the diameter of holes and space of them are almost equal for hexagonal pattern, and the resonance wavelength is 0.866 times of lattice constant ($\lambda \approx \sqrt{3}a/2$). These are easier for fabrication of bigger feature and space sizes at the desired wavelengths compare to square pattern with square holes ($\lambda \approx a$, w/d=0.55~0.6). Moreover, the hexagonal pattern has smaller FWHM compare square pattern.

2. **Reducing the thickness of the metal layer**

   From the fabrication of the proposed devices, we found the most parts of the device are not etched completely. The main reason is the metal layer of standard MicraGEM is too thick (750 nm); DRIE processing is not sure to pass through the metal layer into the silicon layer at the minimum size in the design rules. For the application of the proposed devices, 200 nm is enough for the metal layer to act surface film.

3. **Improving the control ability of the fabrication**

Just as discussion above, the depth of air holes will affect the light extraction efficiency. We can control the etching time of DRIE to obtain the desired depth of air holes. However, the etching rate has a little difference for small size of holes and profile of the device. This is a trial of the fabrication, which needs a lot of experiments to obtain reliable data.

5.3 Future works:

1. Continue to study the interaction between the electromagnetic radiations with PC surface texture technology

Lord Rayleigh in1887 first studied electromagnetic wave propagation in periodic media for one-dimensional photonic crystal. It was not until 100 years later, when Yablonovitch and John in 1987 jointed the tools of classical electromagnetic and solid-state physics, which the omni-directional photonic band gaps in two and three dimensions, was introduced [9]. The PC and surface film technology have recently triggered a lot of interest in connection with their numerous potential technological applications. In this thesis, only some basic foundational research works was done which deals with thermal, electrical, optical and mechanical response. However, some intrinsic electromagnetic radiation interaction in photonic crystal structures, complicated computational methods of electromagnetic field dispersion, such as using the FDTD to solve the time-domain Maxwell's equations in the unit cell, need to be studied.

2. Looking for suitable fabrication technology process

Although MicraGEM standard fabrication process has many advantages for this proposed device, it also has disadvantages, such as thicker metal layer that DRIE is difficult to pass through it into a certain depth of silicon layer. It was unstable when we used minimum feature size of the design rules to design the proposed device. However, in some papers, some group have successfully fabricated hole array samples in a polycrystalline silver film, with film thickness of t=200nm, hole diameter d=150 nm, and a period of a=900nm, for even smaller features to study optical transmission efficiency [13] [14].

3. Measurement experiments

Many conclusions came from the simulation of the proposed structures. They need to be proved by the measurement experiments, such as the absorption, reflection, and emission of light.

References:

1. Brain R. Kinkade, James T. Daly, and Edward A. Johnson, "MEMS-Enabled Intrinsically Safe Infrared Combustible Gas Sensors", 2003
2. Irina Puscasu, "Photonic crystals shrink infrared optical sensors-tracing gases", SPIE -the international society for optical engineering magazine, may 2003
3. I. E1-Kady, R. Biswas, Y. Ye, M. F. Su, I. Puscasu, Martin Pralle, E. A. Johnson, J. Daly, A. Greenwald "Tunable narrow-band infrared emitters from hexagonal lattices" Photonics and Nanostructures- Fundamentals and Applications 1(2003)
4. TEXAS INSTRUMENTS " Patented Virtual Reference Infrared Gas Sensor By Mahesan Chelvayohan, Sensor Design Engineer Texas Instruments, Inc.1999
5. MEMS Optical (Infrared) Gas Sensor, Ion Optics' website- www.ion-optics.com
6. M.U. Pralle, N. Moelders, M.P. McNeal, I. Puscasu, A.c. Greenwald, J.T. Daly, and E. A. Johnson, "Photonic Crystal Enhanced Narrow-band Infrared Emitters", App. Phys. Let. Vol. 81, Num. 25, Dec. 2002
7. Irina Puscasu, Martin U. Pralle, Mark P. McNeal, Nicholas Moelder, Lisa Last, William Ho, Anton C. Greenwald, James T. Daly, Edward A. Johnson, "FREQUENCY SELECTIVE SURFACES ENABLE MEMS GAS SENSOR", Mat. Res. Soc. Symp. Proc. Vol. 722, ©2002 Materials Research Society.
8. Steven G. Johnson and John D. Joannopoulos, "Photonic Crystals-The road from Theory to Practice" Kluwer Academic Publishers, 2002
9. J. Joannopoulos, R. Meade, and J. Winn, "Photonic Crystals" (Princeton

University, Princeton, NJ, 1995).

10. Steven G. Johnson and J.D. Joannopoulos, "Introduction to Photonic Crystals: Bloch Theorem, Band Diagrams, and Gaps (But No Defects), 2003

11. Anton C. Greenwald, James T. Daly, Edward A. Johnson, Brian Kinkade, Mark McNeal, Martin Pralle, and Nicholas Moelders, Thomas George and Daniel S. Choi, Rana Biswas and Ihab E1-Kady, " NARROW BAND EMISSION FROM LITHOGRAPHICALLY DEFINED PHOTONIC BANDGAP STRUCTURES IN SILICON: MATCHING THEORY AND EXPERIMENT" Mat. Res. Soc. Symp. Proc. Vol.637 ©2003 Materials Research Society.

12. Janusz Sadowski, VTT information technology microsensing Biosensors group, http://www.vtt.fi/tte/biosensors/spr.pdf "SPP RESEARCH STATION, A RESEARCH INSTRUMENT BASED ON THE SURFACE PLASMON RESONANCE PHENOMENON".

13. D. E. Grupp, H. J. Lezec, T. W. Ebbesen, K. M. Pellerin and Tineke Thio "Crucial role of metal surface in enhanced transmission through subwavelength apertures, App. Phys. Let, Vol. 77, Num. 11, Sep. 2000

14. H. F. Ghaemi, Tineke Thio, and D. E. Grupp, T. W. Ebbesen, H. J. Lezec, " Surface plasmon enhance optical transmission through subwavelength holes", Phys. Rev. B, Vol. 58, Num. 11, Sep. 1998

15. Biacore AB "Surface plasmon resonance"

16. H. F. Ghaemi, Tineke Thio, and D. E. Gruph, "Surface plasmons enhance optical

transmission through subwavelength holes", Phy. Rev. B, Vol.58, Num.11, 1998-I

17. D.E.Grupp, H.J.Lezec, K.M.Pellerin and Tineke Thio, "Crucial role of metal surface in enhanced transmission through subwavelength apertures." App. Phys. Let. Vol.77, Num.11, 2000

18. M. Parameswaran, H. P. Baltes and A.M. Robinson, "Polysilicon microbridge fabrication using standard CMOS technology", IEEE, 1988.

19. NASA's Jet Propulsion Laboratory, Pasadena, California " Micromachined Emitter/ Bolometer Structures for Infrared Gas Sensors"

20. K. Sakoda, "Optical Properties of Photonic Crystals", Springer, 2001

21. Anton C. Greenwald, Martin U. Pralle, Mark P. NcNeal, Nichoals Moelders, Irina Puscasu, James T. Daly and Edward A. Johnson "Modeling Combined Thermal, Electrical, Optical and Mechanical Response for MEMS Spectroscopic Gas Sensor Based On Photonic Crystals", Mat. Res. Soc. Symp. Proc. Vol.741, ©2003 Materials Research Society.

22. Ivan B. Divliansky, Atsushido, lam-choon, and Theresa S. Mayer, David Pena, Suzushi Nishimura, Chistine D. Keating, and Thomas E. Mallouk "Fabrication of two-dimensional photonic crystals using interference lithography and electrode position of CdSe", App. Phys. Let. Vol. 79, Num.21, American Institute of Physics, Nov. 2001

23. Han-Youl Ryu, Jeong_ki Hwang, Yong-Jae Lee, and Yong-Hee Lee, "Enhancement of Light Extraction From Two- Dimensional Photonic Crystal Slab

Structures", IEEE, 2002

24. RSoft Design Group, Inc. "BandSOLVE 1.3".

25. Rsoft Design Group, Inc. "Rsoft Photonics CAD Layout v5.1.1 User Guide

26. CMC (Canadian Microelectronics Corporation) and Micralyne Inc. "Introduction to MicraGEM: A Silicon- On- Insulator Based Micromaching Process" Report ICI-138, V2.0, Dec. 2003.

27. Rsoft Design Group, Inc. "FullWAVE v3.0.1"

28. A. Taflove, Computational Electrodynamics: The finite-Difference Time-Domain Method. Norwood, MA: Artech, 1995.Microelectromechanical Systems (MEMS)

29. Ben Hiett," Photonic Crystal Moldeling using Finite Element Analysis, 2002

30. Misha Boroditsky, Roberto Coccioli, Eli Yablonovitch, "Analysis of photonic crystals for light emitting diodes using the finite difference time domain technique", phys. Ucla.edu.

31. James Campbell, Luca Cannas, Ghing Yih Chee, Mohanned Eltayeb, Martin Fenner, Gianluca Guiccardi, " Space Applications of Micromachined Silicon", An ISE2 Group Project Report (2003)

32. Ion Inc. " Applied MEMS to provide packing foundry services for ION"

33. Microelectromechanical systems (MEMS)

34. Vladimir Poborchii, Tetsuya Tada, and Toshihiko Kanayama, Alexander Moroz "Silver-coated silicon pillar photonic crystals: Enhancement of a photonic band gap" App. Phys. Let. Vol. 82, Num.4, Jan. 2003

35. Shanhui Fan, Pierre R. Villeneuve, J. D. Johnnopoulos, E. F. Schubert "High Extraction Efficiency of Spontaneous Emission from Slabs of Photonic Crystals" Phys. Rev Lets. Vol. 78,Num. 17, Apr. 1997

36. Alexei A. Erchak, Daniel J. Ripin, Shanhui Fan, John D. Joannopoulos, Erich P. I ppen, Gale S. Petrich, and Leslie A. Kolodziejski, "Enhanced Emission from a Light-Emitting Diode Modified by a Photonic Crystal" Mat. Res. Soc. Symp. Proc. Vol.637 ©2001 Materials Research Society.

37. Alexei A. Erchak, Daniel J. Ripin, Shanhui Fan, Peter Pakich, John D. Joannopoulos, Erich P. Ippean, Gale S. Petrich and Leslie A. Kolodziejski " Enhanced coupling to vertical radiation using a two- dimensional photonic crystal in a semiconductor light- emitting diode" App. Phs. Let. Vol. 78,Num 5, Jan. 2001

38. M. U. Pralle et all. "Photonic crystals for narrow-band infrared emission," SPIE proceedings vol. 4574, (2002)

Appendix 1

Measurement methods for the proposed devices

The spectra measurements can be acquired using Fourier Transform Infrared (FTIR) spectroscopy (such as Nicolet Nexus 670 spectrometer) with attenuated total reflectance (ATR) accessories (showed in Fig. AI.1). The theory description is that the incident light with intensity, I_0 upon a sample and after interacting with that sample (either transmitted, reflected or absorbed) has some lower intensity, I. The intensity as a function of frequency (the infrared spectrum) offers a fingerprint of the chemical bonds present within the material. The reflection measurement was carried at room temperature and normal incident, in the range of 7000-500 cm^{-1} at a resolution of 4 cm^{-1}. The aperture in the sample stage was chosen to be just smaller than the area of the area of the photonic crystal patterns. The sample spectrum was referenced to a gold standard to remove the effects caused by the ambient atmosphere [7].

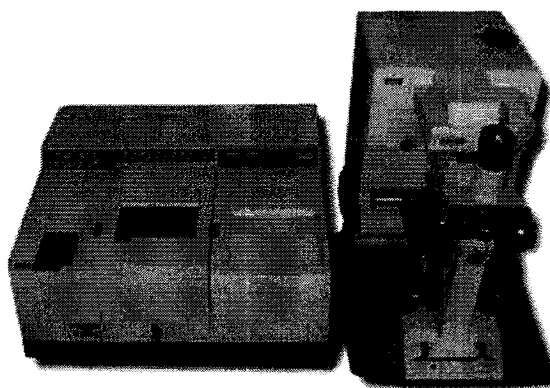

Figure AI.1 FTIR with microscope

According to energy conservation, the absorption is $A = 1 - R - T \cong 1 - R$, since

the transmission through the substrate is eliminated in the calculations. Experimentally, $A \cong 1 - R$ since negligible transmission is observed through the thick gold-coated silicon wafer. A sharp peak complementary to reflectivity calculation thus characterizes the absorption spectrum. By Kirchoff's law, the emission of the structure is equal to the absorption (A) weighted by the blackbody emissive ($K(\upsilon,T)$) at the temperature T of the measurement. Emission and absorption of the radiation are related processes. Emission and absorption of the radiation are related processes [3].

$$E(\upsilon,T) = A(\upsilon)K(\upsilon,T), \qquad k(\upsilon,T) = \frac{8\pi h\upsilon^3 / c^3}{e^{h\upsilon/kT} - 1} \tag{4-1}$$

For emission measurements, samples are heated to $325^{o}C$ on a hot stage for several minutes to ensure they reached set point temperature. The infrared radiation is collected, using a parabolic right angle mirror and imaged into the interferometer.

Appendix II

The FDTD Algorithm: Finite Difference Time Domain (FDTD) methods [27-30]

The main reason for choosing the FDTD method is to account for dispersion, loss, nonlinearity, and metallic materials in the crystal, which cannot be included in the plane wave treatment. The FDTD method may also be faster in isolating certain modes at very high band numbers.

The FDTD is a rigorous solution to Maxwell's equations and does not have any approximations or theoretical restrictions. This method is widely used as a propagation solution technique in integrated optics.

Imagine a region of space, where which contains no flowing currents or isolated charges. Maxwell's curl equations in can be written in Cartesian coordinates as six simples scalar equations. Two examples are:

$$\frac{\partial Hx}{\partial t} = -\frac{1}{\mu}\left[\frac{\partial Ey}{\partial z} - \frac{\partial Ez}{\partial y}\right]$$

$$\frac{\partial Ey}{\partial t} = -\frac{1}{\mu}\left[\frac{\partial Hx}{\partial z} - \frac{\partial Hz}{\partial x}\right] \qquad \text{(AII-1)}$$

The other four are symmetric equivalents of the above and are obtained by cyclically exchanging the x, y and z subscripts and derivatives.

Maxwell's equations describe a situation in which the temporal change in the E field is dependent upon the spatial variation of the H field, and vice versa. The FDTD method

solves Maxwell's equations by first discrediting the equation via central differences in time and space and then numerically solving these equations in software.

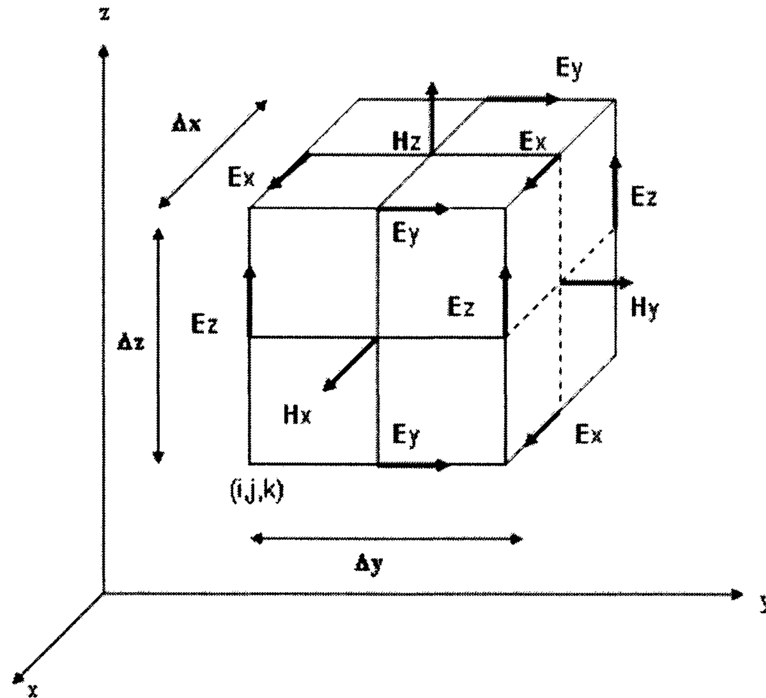

Figure AII.1 The E and H field components are then interlaced in all three spatial dimensions

The most common method to solve these equations is based on Yee's mesh and computes the E and H field components at points a grid with grid points spaced Δx, Δy, and Δz apart. The E and H field components are then interlaced in all three spatial dimensions as shown in Fig.38. Furthermore, time is broken up into discrete steps of Δt. The E field components are then computed at times t=n Δt and the H fields at times t= (n+1/2) Δt,

where n is an integer representing the compute step. For example, the E field at a time t=n Δt is equal to the E field at t= (n-1) Δt plus an additional term computed from the spatial variation, or curl, of the H field at time t.

This method results in six equations that can be used to compute the field at a given mesh point, denoted by integers i, j, k. For example, two of the six are:

$$Hx^{n+1/2}_{x(i,j,k)} = H^{n-1/2}_{x(i,j,k)} + \frac{\Delta t}{\mu \Delta z}(E^{n}_{y(i,j,k)} - E^{n}_{y(i,j,k-1)}) - \frac{\Delta t}{\mu \Delta y}(E^{n}_{z(i,j,k)} - E^{n}_{z(i,j-1,k})$$

$$E^{n+1}_{x(i,j,k)} = E^{n}_{x(i,j,k)} + \frac{\Delta t}{\varepsilon \Delta y}(H^{n+1/2}_{z(i,j+1,k)} - H^{n+1/2}_{z(i,j,k)}) - \frac{\Delta t}{\varepsilon \Delta z}(H^{n+1/2}_{y(i,j,k+1)} - H^{n+1/2}_{y(i,j,k)}) \quad \text{(AII-2)}$$

These equations are iteratively solved in a leapfrog manner, alternating between computing the E and H fields at subsequent Δt/2 intervals.

--Refractive Index Distribution

In order to use the algorithm to study the propagation of light fields in a structure, the refractive index distribution n (x, y, and z) as well as any other relevant material properties of the structure itself must be specified. The simulation utilizes the following formula to specify the material properties of a waveguide:

$$D = \epsilon_0 \epsilon_\infty E + \epsilon_r(\omega) \epsilon_0 E + 2\epsilon_0 n n_2 \frac{I}{1+\frac{I}{I_{sat}}} E \quad \text{(AII-3)}$$

This equation has three terms, each of which corresponds to a different effect. The first term takes into account the linear index of the system. The second term takes into account

material dispersion, or the change of index as a function of wavelength. The final term in this equation is a non-linear term, and is a function of the intensity in the medium.

-- Electromagnetic field excitation:

In order to perform a simulation, an initial launch condition ϕ_L at time t=0 is needed, as well as driving function in time. This consists of both a spatial and temporal excitation, such as:

$$\phi_L(r,t) = f(r_0)g(t) \qquad \text{(AII-4)}$$

Where the spatial excitation at the launch plane is $f(r_0)$, and $g(t)$ is the temporal excitation.

--Boundary conditions

The boundary conditions at the spatial edges of the computational domain must be carefully considered. Many simulations employ an absorbing boundary condition that eliminates any outward propagating energy that impinges on the domain boundaries. One of the most effective is the Perfectly Matched layer (PML), in which both electric and magnetic conductivities are introduced in such a way that the wave impedance remains constant, absorbing the energy without inducing reflections. This allows field energy, which is incident on the boundary to efficiently, leave the domain.

Periodic boundary conditions (PBC) are also important, because of their applicability to PBG structures. There are a number of variations on the PBG, but they share the same common thread: the boundary condition is chosen such that the simulation is equivalent to an infinite structure composed of the basic computational domain repeated endless in

all dimensions. PBC are most often employed when analyzing periodic structures.

They are quite useful when working with period structure types. A period boundary stipulates that any field, which leaves the boundary on one side of the domain, should reenter the domain on the opposite side. This can be expressed mathematically as:

$$E(\chi_i) = E(\chi_i + \Delta)e^{ik_i\chi_i} \qquad \text{(AII-5)}$$

Where the structure is assumed to be periodic along the coordinate χ_i with period Δ and a phase difference k_i, the length of the domain along the specified coordinate χ defines the period $_i$.

--The Spatial and Temporal Grid

In order to produce an accurate simulation, the spatial grid must be small enough to resolve the smallest feature of the field to be simulated. Usually this is dictated by the wavelength in the materials to be simulated, but, in some cases, can be dictated by the geometry of the photonic device. Typically, the grid spacing must be able to resolve the wavelength in time, and therefore usually be less than λ/10 where λ is not the free space wavelength, but rather the wavelength in the materials.

Since the FDTD algorithm is based in the time domain, the simulation has several parameters that relate to temporal grid. To obtain a stable simulation, one must adhere to the Courant condition that relates the spatial and temporal step size:

$$C\Delta t\angle\frac{1}{\sqrt{(\frac{1}{\Delta x^2}+\frac{1}{\Delta y^2}+\frac{1}{\Delta z^2})}} \qquad \text{(AII-6)}$$

Where the velocity of light is C. Note that: all times must be specified as cT in units of μm.